Understanding gas mixing in the circumgalactic medium

Hilay Shah [1,2]★ Freeke van de Voort,[2] Amit Seta[1] and Christoph Federrath[1,3]

[1]*Research School of Astronomy and Astrophysics, Australian National University, Canberra ACT 2611, Australia*
[2]*School of Physics & Astronomy, Cardiff University, Queens Buildings, The Parade, Cardiff CF24 3AA, UK*
[3]*Australian Research Council Centre of Excellence in All Sky Astrophysics (ASTRO3D), Canberra, ACT 2611, Australia*

ABSTRACT

We study gas mixing in a simulated Milky Way–mass galaxy's circumgalactic medium (CGM) using cosmological 'zoom-in' simulations. We insert tracer dyes in the CGM with different gas flows (shearing, coherent, and static) and diverse physical properties to track gas mixing. We correlate the extent and shape of the dye spread with the local gas properties to understand gas mixing. Velocity dispersion and traceless symmetric shear tensors (pure shear deformation) in small regions ($\lesssim 5\,\text{kpc}$) around the dye injection locations best predict the dye spread extent after 200 Myr. We use this to determine diffusion calibration constants for subgrid-scale mixing models. While the dye shape after 200 Myr aligns well with the velocity dispersion and magnetic field dispersion, the best alignment occurs with the dispersion of stretching eigenvectors (traceless symmetric shear tensor) and plane of rotation (antisymmetric shear or vorticity tensor) in large regions ($\gtrsim 10\,\text{kpc}$) around the dye injection locations. Therefore, shear statistics and velocity dispersion best predict the extent and shape of mixed gas. The linear temporal dependence of the dye spread suggests superdiffusion in the CGM, potentially due to turbulent and large-scale coherent flows or numerical diffusion. Despite significant numerical mixing from our 1 kpc resolution (insufficient to resolve Reynolds numbers $\sim 10^2$–10^3, which require a few hundred pc resolution), our correlation results are robust thanks to fixed spatial resolution throughout the CGM. These results can be used to predict diffusion coefficients to model magnetic field diffusion, heat transport, and metal mixing.

Key words: MHD – turbulence – methods: numerical – galaxies: haloes – galaxies: magnetic fields.

1 INTRODUCTION

The multiphase circumgalactic medium (CGM) links the interstellar medium (ISM) of galaxies with the diffuse intergalactic medium (IGM). This gas reservoir extends out to about the virial radius of the dark-matter-dominated halo [$\sim 200\,\text{kpc}$ for a Milky Way (MW)–mass system] and interacts with the enriched outflows from star-forming discs and pristine inflows from the IGM. The cool gas flows accreting from the CGM to the ISM provide the fuel for future star formation. The CGM also contains most of the metals expelled from the ISM. It is thus key to answering questions of sustained star formation (Heavens et al. 2004; Bigiel et al. 2011; Kennicutt & Evans 2012; Putman 2017), missing baryons (McGaugh et al. 2009; Behroozi, Conroy & Wechsler 2010), and missing metals in galaxies (Tremonti et al. 2004; Peeples et al. 2014). The physical properties of the CGM indirectly influence feedback processes, affecting how galaxies evolve and the resulting outflows (Tumlinson, Peeples & Werk 2017; Crain & van de Voort 2023; Faucher-Giguère & Oh 2023b). Therefore, it is vital to understand its properties and underlying physical processes to understand and test theories of galaxy formation and evolution and interpret observations (Tumlinson et al. 2017).

Various physical processes around the CGM make it a multiphase medium. Some major mechanisms include the supernovae-driven hot outflows from the galaxy (Thompson et al. 2015; Fielding et al. 2017), the cool inflows from the IGM or thermal instabilities (McCourt et al. 2012), mixing between different layers of the cold clouds ejected by galactic wind (Begelman & Fabian 1990; Grønnow, Tepper-García & Bland-Hawthorn 2018; Das & Gronke 2023), cooling induced by stripping of massive satellites (Roy et al. 2024), and cool gas swept up in wakes of satellites (Saeedzadeh et al. 2023). The presence of diffuse hot coronae ($T \sim 10^6\,\text{K}$) has been theoretically predicted by cosmological theories (Spitzer 1956; Fukugita, Hogan & Peebles 1998; Fukugita & Peebles 2006; Stinson et al. 2012). Deep X-ray absorption observations have revealed warm, warm-hot, and hot phases of the CGM (Das et al. 2021). The O VI, O VII, and O VIII absorption and emission lines provide evidence for this hot component (Tumlinson et al. 2011; Miller & Bregman 2015; Locatelli et al. 2024). The hot phase can also be indirectly probed by the interaction of the Magellanic stream with the hot coronal MW gas (Mastropietro et al. 2005; Gaensler et al. 2008; Fox et al. 2010). The cold component ($T \leq 10^4\,\text{K}$) is present in the form of high-velocity clouds, detected mainly by H I, Si II, Mg II observations (Wakker & van Woerden 1997; Wakker et al. 2007; Shull et al. 2009; Steidel et al. 2010; Kacprzak & Churchill 2011; Werk et al. 2014). Through cooling of hot gas or mixing of the interface of these clouds with the hot coronal surroundings warm ionized gas is generated ($T \sim 10^5\,\text{K}$) (Kwak, Henley & Shelton 2011; Armillotta et al. 2017).

Gas turbulence causes mixing and perturbations of density and temperatures, which influences CGM's multiphase dynamics (Seta & Federrath 2022; Das & Gronke 2023). Understanding turbulent mixing in the CGM can thereby elucidate a variety of gas interactions and properties – inflows and outflows mixing with the CGM (Pakmor et al. 2020; Faucher-Giguere & Oh 2023a), mass outflow rates (Muratov et al. 2017; Mitchell et al. 2020), and the chemical composition of the ambient CGM interacting with metal-rich outflows. Through mixing, the metal-rich outflows are diluted, while the metal-poor CGM becomes relatively metal rich (Faucher-Giguere & Oh 2023a). This alteration in metallicities changes the gas cooling properties, thereby affecting the properties of gas accretion and wind recycling (Hafen et al. 2020), which can be crucial in understanding the galaxy stellar mass function (Oppenheimer et al. 2010).

The limited resolution in all simulations means that realistic astrophysical Reynolds numbers (Re) of order $\gtrsim 10^7$ are challenging to simulate (Garnier, Adams & Sagaut 2009). It is also not trivial to understand the effects of changing resolution – both idealized (Scannapieco & Brüggen 2015; Schneider & Robertson 2017; Sparre, Pfrommer & Vogelsberger 2018) and cosmological simulations predict that the properties of the CGM change substantially with resolution. For instance, stellar mass and H I column densities change with resolution in cosmological simulations (Murante et al. 2014; Pakmor et al. 2015; Hopkins et al. 2018; Hummels et al. 2019; Peeples et al. 2019; van de Voort et al. 2019; Grand et al. 2021). Gas mixing is one fundamental process that changes with resolution (Banda-Barragán et al. 2018; van de Voort et al. 2021) because resolving the turbulent processes with better resolution reduces the numerical viscosity and diffusion, and models the cascade from larger to smaller scales of eddies better, effectively changing the turbulent viscosity (Kemenov, Wang & Pope 2011; Valdarnini 2011; Landau & Lifshitz 2013; Schmidt 2015). Mesh-based codes usually rely on implicit mixing models rather than explicit models (for subgrid-scale mixing) used in particle-based codes (no mixing unless there is a subgrid model). Given enough resolution, one could identify the gas properties that cause mixing in codes with implicit mixing schemes and use them to calibrate explicit subgrid-scale mixing models. The difference in the numerical techniques changes the modelling of the turbulent cascade significantly (Bauer & Springel 2012), and the need for different mixing models stems from the infeasibility to perform direct numerical simulations for astrophysical scenarios due to high Re (computational effort $\propto Re^4$; Meneveau & Katz 2000).

There are several tricks for simulating the unresolved small-scale turbulent mixing. Large eddy simulations separate large and small scales using a spatial filter and subgrid models with an explicit turbulent viscosity or diffusivity for the unresolved gas mixing (Leonard 1975; Rogallo & Moin 1984; Lesieur & Metais 1996; Meneveau & Katz 2000; Sagaut 2006; Garnier et al. 2009; Schmidt 2015). The Smagorinsky model, which assumes that velocity shear fluctuations drive turbulent mixing, is a commonly adopted subgrid model due to its simplicity (Smagorinsky 1963; Schmitt 2007; Shen, Wadsley & Stinson 2010; Shen et al. 2013; Brook et al. 2014; Williamson, Martel & Kawata 2016; Tremmel et al. 2017; Escala et al. 2018; Sokołowska et al. 2018).[1] Wadsley, Veeravalli & Couchman (2008) implemented the Smagorinsky model and another simple model based on velocity differences in a smoothed-particle hydrodynamics (SPH) code for kinetic and thermal energy dissipation, respectively, to obtain more accurate results. The inclusion of metal diffusion modelling in Shen et al. (2013) as opposed to Shen et al. (2012) increased the spread of heavy elements from outflowing wind material to the surroundings (Shen et al. 2010). The Smagorinsky model, however, results in inaccuracies (e.g. overmixing, incompressibility, modelling supersonic flows due to the presence of shearing shocks), as it fails to describe a scale- and time-dependent diffusivity, because it was derived for highly non-magnetized subsonic flows without a bulk shear. As none of these assumptions hold in the ISM and CGM of galaxies, alternative models have been proposed and implemented recently.

Colbrook et al. (2017) found superdiffusive mixing in supersonic turbulent ISM-like conditions; stressing the need to calibrate the Smagorinsky constant for non-turbulent, anisotropic, and non-shearing flows outside the inertial range of turbulence. They found that the effective diffusivity is proportional to the Mach number (also proportional to the local velocity dispersion) of the fluid (see also Greif et al. 2009; Williamson et al. 2016). Similarly, Rennehan et al. (2019) showed, with the help of isolated galaxy and cosmological simulations using Lagrangian techniques (SPH and meshless finite-mass methods), that the problems associated with the Smagorinsky model can be resolved if the Smagorinsky constant is a function of space and time (Germano et al. 1991). Rennehan (2021) highlighted how an explicit anisotropic eddy viscosity model for metal mixing in Lagrangian cosmological simulations impacts early galaxy evolution and alters metal distributions in circumgalactic gas. Huang et al. (2022) used a different subgrid model calibrated from higher resolution cloud simulations and found a skewed but unimodal CGM metallicity distribution. The nature of mixing in the CGM radically alters the metallicity distributions; thus, it is crucial to understand the nature of mixing in realistic CGM-like conditions that include magnetic fields. Thus, we aim to validate the typical mixing scalings using our cosmological simulations with implicit mixing and magnetic fields, which are of great dynamical importance in galaxies.

Two main scenarios for the presence of magnetic fields are that large-scale outflows carry them from the ISM into the CGM (Pakmor et al. 2020; Arámburo-García et al. 2023; Heesen et al. 2023; Ramesh et al. 2023) or that a turbulent dynamo operates within the CGM (Beck et al. 2012; Marinacci et al. 2015; Pakmor et al. 2017, 2020). As a result, magnetic field strengths of 0.1–1 µG are observed up to impact parameters of a few tens of kpc from the galaxy discs into the CGM (Bernet, Miniati & Lilly 2013; Lan & Prochaska 2020; Amaral, Vernstrom & Gaensler 2021; Shah & Seta 2021; Böckmann et al. 2023). Voort et al. (2021) showed the results of cosmological simulations of MW–mass galaxies with and without magnetic fields, which indicate that magnetic fields have a strong influence on CGM dynamics. On a fundamental level, magnetic fields can directly affect mixing in the CGM by suppressing Kelvin–Helmholtz instabilities, leading to a reduced formation of cool gas from the lack of intermediate temperature gas (Chandrasekhar 1968; Ji, Oh & Masterson 2019; Das & Gronke 2023; Jennings et al. 2023). In general, magnetic fields have been shown to reduce the required turbulent pressure support by providing magnetic pressure support (Mohapatra et al. 2021a, b), thus suppressing turbulent mixing. Therefore, including magnetic fields, as we do in this work, is important for studying the gas mixing properties of the CGM (Pakmor et al. 2020; Voort et al. 2021).

In this work, we use cosmological 'zoom-in' simulations of a single MW-mass halo with enhanced resolution in the CGM (Voort et al. 2021). We study the mixing of tracer dyes to understand the dependence of gas mixing on the physical properties of the CGM.

---

[1]This is related to Boussinesq eddy viscosity hypothesis (Schmitt 2007), Reynolds stress tensors (Reynolds 1895), and Prandtl mixing length theory (Prandtl 1925; Landau & Lifshitz 2013).

The simulation method and the selection of tracer dye locations are described in Section 2. In Section 3, we present the results showcasing the correlation of gas mixing with various gas properties, effects of limited resolution, and turbulent properties of the CGM. We summarize our findings in Section 4.

2 METHODS

2.1 Simulations

This work utilizes simulations from the Simulating the Universe with Refined Galaxy Environments (SURGE) project (see also de Voort et al. 2019), using the same initial conditions and galaxy formation model as the Auriga simulations, a suite of cosmological zoom-in simulations of MW-like galaxies (Grand et al. 2017; Voort et al. 2021). They were run with the AREPO code, which employs moving-mesh techniques based on a Voronoi mesh (Springel 2010; Pakmor et al. 2015; Weinberger, Springel & Pakmor 2020). This quasi-Lagrangian scheme offers several benefits over other commonly used Eulerian (fixed mesh) codes with or without adaptive mesh refinement (AMR) and SPH codes. It improves upon suppressed fluid instabilities in SPH (Sijacki et al. 2012) and Galilean non-invariance and the presence of overmixing in Eulerian codes (Springel 2010). Additionally, several benefits of SPH (e.g. low numerical diffusion) and Eulerian (e.g. good convergence for smooth flows, capturing shocks accurately) codes are retained in these moving-mesh techniques (Dale 2015; Pakmor et al. 2015). Thus, moving mesh techniques should provide a more accurate physical description of gas mixing in the CGM (Duffell & MacFadyen 2011).

For this study, we selected one of the Auriga galaxies (halo 12)[2] and resimulated it using standard mass refinement only (Voort et al. 2021) and using standard mass refinement combined with fixed additional spatial refinements (1 kpc and 2 kpc). For all simulations, there is a standard mass refinement such that the target cell masses for baryons and dark matter particles are $5.4 \times 10^4 \, \mathrm{M_\odot}$ and $2.9 \times 10^5 \, \mathrm{M_\odot}$, respectively. For the runs with minimum 1 and 2 kpc spatial resolutions, an additional volume refinement criterion is included within $1.2 R_{\mathrm{vir}}$, which is dominant when $\rho < \rho_{\mathrm{threshold}}/64$ and $\rho < \rho_{\mathrm{threshold}}/512$[3], respectively. This translates to a maximum cell size of ~ 1 and 2 kpc and a maximum cell volume of ~ 1 and $8 \, \mathrm{kpc^3}$ inside $1.2 R_{\mathrm{vir}}$, respectively. Here, we define the virial radius (R_{vir}) as the radius within which the mean overdensity (ρ_{over}) is 200 at its redshift, where ρ_{over} is the density divided by the critical density of the universe. Mass refinement is dominant when $\rho > \rho_{\mathrm{threshold}}/64$ and $\rho > \rho_{\mathrm{threshold}}/512$, leading to spatial resolutions ≤ 1 and 2 kpc overall, respectively. The majority of our results use 1 kpc resolution runs, and the 2 kpc runs are used only for the convergence tests and checking the results' robustness (see Section 3.5). The selected halo has $R_{\mathrm{vir}} \approx 213 \, \mathrm{kpc}$ at $z \approx 0.059$ (subsequent analyses performed at or after this redshift), and the total virial mass of the main halo is $10^{12} \, \mathrm{M_\odot}$.

The simulations were run with the latest version of AREPO while adopting a ΛCDM (Lambda cold dark matter) cosmology with parameters taken from Planck Collaboration et al. (2014): $\Omega_{\mathrm{m}} = 1 - \Omega_\Lambda = 0.307$, $\Omega_{\mathrm{b}} = 0.048$, $h = 0.6777$, $\sigma_8 = 0.8288$, and

$n = 0.9611$. Except for the additional spatial refinement, we use the same physical model as the original Auriga simulations (Grand et al. 2017). However, mass and metals ejected by a star particle are injected only into its host cell rather than its 64 neighbouring cells as in Grand et al. (2017). This is not expected to bring significant differences within the scope of this study because metals quickly mix with surrounding gas and there are numerous such metal injection events (supernovae) that both methods would yield statistically similar results (see de Voort et al. 2020, who studied the difference in the context of rare rapid neutron capture elements and found negligible impact). It should be noted that momentum injection is still performed in the same way as the original Auriga simulations with wind particles, so outflow properties are not altered. Furthermore, the gas we study is so far away in the CGM that the precise details of the metal injection methodology would not affect the CGM properties.

2.2 Dye location selection

To understand gas mixing in different environments of the CGM, we implement tracer dyes (referred to as 'dye' hereon) in our simulations. The dye is a passive scalar that advects with the fluid. To initialize the dye, we select cells according to the criteria given in Section 2.2.2 at $z \approx 0.059$, inject the dye, and restart the simulation from that point with outputs saved every 10 Myr. The selected cells for dye injection are assigned with a scalar value of 1, the rest being 0. At any later time in a given cell, the mass fraction of the initially injected dye can be determined by the scalar value in that cell. Thus, it allows us to track and analyse gas transport between the computational cells. Previously, a similar methodology has been adopted in other simulations with different terminology, for instance, pollutants in Pan, Scannapieco & Scalo (2012), passive tracers in Grønnow et al. (2018), and passive scalars in Schneider et al. (2020). This dye allows us to track the entire distribution of mixed gas, useful for studying advection and diffusion processes.

2.2.1 CGM classification

To capture the multiphase nature of the CGM, we inject the dye in 95 cells at locations representing different local environments with different physical properties at $z = 0.059$ and create outputs with 10 Myr spacing for a total of 200 Myr. First, we average gas properties into a uniform 3D grid, centred on the galaxy, with dimensions $400 \times 400 \times 400$ kpc. The 3D voxels are $10 \times 10 \times 10$ kpc cubes that inherit averaged gas properties from the gas cells within each region. Each $(10 \, \mathrm{kpc})^3$ voxel contains $\sim 10^3$ cells as the individual cell sizes are ~ 1 kpc; thus, 10 kpc voxel gas properties are determined using either averages or the sum of different gas properties of cells inside the voxel. The volume-weighted average is used for temperatures, densities, and metallicities, the mass-weighted average is used for radial velocities and velocities, and the sum is used for kinetic energy.

All the voxels with overdensities (ρ_{over}) ≥ 150 are ignored in selection to avoid choosing the ISM or disc–halo interface gas of either the host or the satellite galaxy, and make the selection sufficiently far into the CGM ($\gtrsim 20$ kpc from the galactic centre). Voxelating prevents identifying different environments based on fluctuations at individual cell scales and selects regions based on their 10 kpc local-scale properties. All the gas properties concerning the voxels are represented with a 'v' in the superscript. For instance, the radial (total) velocity of an individual AREPO cell is denoted as V_{rad} (V), while that for the interpolated voxel is denoted V_{rad}^v (V^v).

[2]Information on the basic properties of simulated haloes with standard resolution is available at https://wwwmpa.mpa-garching.mpg.de/auriga/about.html. Details of halo 12 can be found in Grand et al. (2017) and Voort et al. (2021) [3]$\rho_{\mathrm{threshold}}$ is the gas density above which star formation occurs, i.e. $n_{\mathrm{H}}^\star = 0.11 \, \mathrm{cm^{-3}}$.

i − inflows, s − static flows, o − outflows, a − azimuthal flows
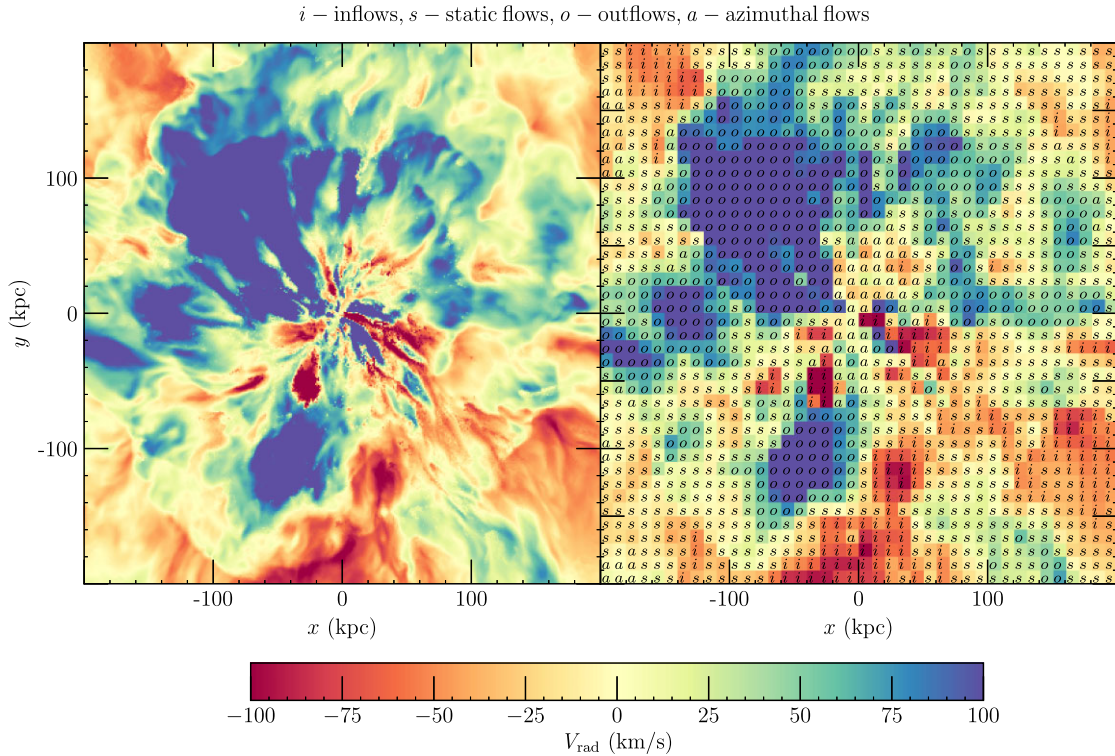
Figure 1. *Left*: 10 kpc deep (along the line-of-sight) projection through the halo centre of the radial velocity with standard mass resolution + 1 kpc refinement in a box of $400 \times 400 \times 10$ kpc. *Right*: Radial velocity of the voxelated (voxel size = $10 \times 10 \times 10$ kpc) CGM in a 400×400 kpc image. The text in the centre of every voxel shows the flow type (see title) of the voxel based on its radial and total velocities (see Section 2.2.1). The galaxy is shown in the (random) coordinate frame of voxel selection, not edge-on as in subsequent figures.

Fig. 1 (left panel) shows a thin projection of the radial velocities with strong outflows in blue and inflows in red. The right panel is the voxelization of the left panel. We further characterize the voxels into inflows, outflows, static, and azimuthal flows locally using the following criteria. We define $|V_{\rm rad}^v| > 40$ km s^{-1} as either an inflow ($V_{\rm rad}^v$ is negative) or an outflow ($V_{\rm rad}^v$ is positive). And when $|V_{\rm rad}^v| < 40$ km s^{-1}, it is defined as either a static flow ($|V^v| < 80$ km s^{-1}) or an azimuthal flow ($|V^v| > 80$ km s^{-1}). Static flows are relatively static regions. The net inflow and outflow velocities have magnitudes of ~ 50 km s^{-1} in the presence of magnetic fields in the CGM (see fig. 6 in Voort et al. 2021). As outflows would slow down due to entrainment as they reach the outer CGM, we select a 40 km s^{-1} radial velocity cut-off. The total velocity cut-off of 80 km s^{-1} is chosen to differentiate whether the non-radial gas has a strong component in the azimuthal direction.

2.2.2 Dye injection location based on flow interactions and gas properties

We identify locations for dye injection based on flow interactions: interacting inflows-outflows (io), pure inflows (i), pure outflows (o), pure static flows (s), and outflows interacting with static flows (os):

(i) Interacting inflows-outflows (io): To find these, we examine voxels representing inflow and outflow regions nearby, specifically within a distance equal to twice the voxel diagonal ($20\sqrt{3}$ kpc). Assuming constant velocities, we track their trajectories to determine the points of the closest approach. We ensure that this occurs within a reasonable time-frame (~ 150 Myr). The interaction is confirmed

if both voxels reach their closest points nearly simultaneously. This method ensures that only plausible inflow–outflow interactions are considered. We select both the inflow and outflow voxels from an inflow–outflow pair but dye them with separate colours. Different dye colours refer to different initialized passive scalars, allowing them to track the dye independently of one another. More details can be found in Section A.

(ii) Pure inflows (i), outflows (o), and static flows (s): If more than 90 per cent of the voxels in a region of $50 \times 50 \times 50$ kpc are classified as a single flow type (see Section 2.2.1) along with the central voxel, then the central voxel is selected as a pure inflow, outflow, or a static flow, depending on the majority of the flow type in that region.

(iii) Outflows interacting with static flows (os): To select static flows with outflow interaction at a later time, we first find voxels with strong outflows ($V_{\rm rad} > 100$ km s^{-1}). Then we select regions of $50 \times 50 \times 50$ kpc around the strong outflows with static flows ≥ 30 per cent, outflows ≥ 50 per cent, and inflows ≤ 5 per cent, to locate regions with substantial outflows and static flows. The static voxel whose position vector (from the centre of the strong outflow) has the smallest angle with the strong outflow velocity vector inside a region of $50 \times 50 \times 50$ kpc is selected as os.

Finally, we select an individual cell (i.e. one resolution element) inside each voxel ($10 \times 10 \times 10$ kpc region) to inject the dye. We only consider individual cells with gas properties (T, Z, and KE) in similar ranges (low or high) as their respective voxels. For interacting inflows-outflows, the cells (one from inflow and one from outflow voxel) closest to each other are selected. For pure flows, the cell closest to the centre of the voxel is selected. For outflows interacting

Table 1. Properties and statistics of the dye injection locations in the CGM. For gas properties, 'L' refers to low, 'H' refers to high, and 'N/A' refers to a random selection. The columns are as follows: 1: number of the dye colour, 2: type of flow interaction, 3: number of separate dye injection cells, 4: temperature selection, 5: kinetic energy selection, 6: metallicity selection. In total, 95 different cells are selected.

N_{col}	Flow interactions	No. of dye injection cells	T	KE	$Z/Z_\odot$
0	Inflows in interacting inflows $-$ outflows (*io*)	4	L	L	L
1	Inflows in interacting inflows $-$ outflows (*io*)	2	L	H	H
2	Inflows in interacting inflows $-$ outflows (*io*)	2	L	L	L
3	Inflows in interacting inflows $-$ outflows (*io*)	4	H	L	L
4	Inflows in interacting inflows $-$ outflows (*io*)	4	H	H	H
5	Outflows in interacting inflows $-$ outflows (*io*)	4	H	L	L
6	Outflows in interacting inflows $-$ outflows (*io*)	2	H	H	H
7	Outflows in interacting inflows $-$ outflows (*io*)	2	L	L	L
8	Outflows in interacting inflows $-$ outflows (*io*)	4	H	L	L
9	Outflows in interacting inflows $-$ outflows (*io*)	4	H	H	H
10	Pure inflows (*i*)	4	L	L	L
11	Pure inflows (*i*)	4	L	H	H
12	Pure outflows (*o*)	4	H	L	L
13	Pure outflows (*o*)	3	H	H	H
14	Pure static flows (*s*)	4	L	L	L
15	Pure static flows (*s*)	4	L	L	H
16	Pure static flows (*s*)	4	L	H	L
17	Pure static flows (*s*)	4	L	H	H
18	Pure static flows (*s*)	4	H	H	L
19	Pure static flows (*s*)	4	H	H	H
20–25	Outflows interacting with static flows (*os*)	24	N/A	N/A	N/A

with static flows, the cell (from the static flow voxel) closest to and in the direction of the strong outflow is selected. The dye injection cells in a specific colour are separated by at least 60 kpc to ensure no overlap. Table 1 shows the dyed cells' gas properties and flow interaction types based on our selection criteria. No. of dye injection cells refers to the number of cells dyed with one colour. 'L' (bottom 33 percentile) and 'H' (top 33 percentile) refer to low and high values for those gas properties. 'N/A' refers to a random selection because the sample size was not large enough to subdivide into different gas properties. In total, 95 cells are dyed with 26 different dye colours. The procedures described in this section ensure a sample with diverse flow interactions and varying gas properties.

Fig. 2 shows five dyed cells, with the top panels showing their locations and different gas properties at the injection time. Numbers 1–5 (in the top panels) represent one dye injection cell from each flow interaction type – 1: interacting inflow–outflow, 2: pure inflow, 3: pure outflow, 4: pure static flow, and 5: outflow interacting with static flow. The bottom panels show the evolution of dye mass fraction over 200 Myr at six different times. The dye mixes more in the interacting inflow-outflow case (more shearing) while mixing is relatively slower in pure (more coherent) flows. Thus, there could be some dependence of dye mixing on the gas velocity statistics.

Fig. 3 compares the probability density functions (PDF) of gas properties of the dyed cells (95 in number) and overall CGM gas (cells between $50 < r < 200$ kpc). Both PDFs look very similar for all gas properties. The dyed cells' standard deviations (given in each panel) are usually somewhat higher than or almost equal to the standard deviations of the CGM gas. This shows that the 95 cells selected for dye injection represent a diverse environment of the CGM in terms of various gas properties like density, temperature, magnetic fields, kinetic energy density, and metallicity. Note that we represent gas densities using two quantities throughout the text – hydrogen number density (n_H) and overdensity (ρ_{over}). Multiplying n_H with a factor of 2.44×10^5 approximately converts it to ρ_{over}.

3 CORRELATING GAS MIXING WITH PHYSICAL PROPERTIES

To understand gas mixing in the CGM, we first quantify how much the dye mixes and spreads in its environment. We study the surroundings (up to 60 kpc) of the dye injection region, centred on the cell with the largest dye mass fraction. The $60 \times 60 \times 60$ kpc region is divided into 40 $1.5 \times 60 \times 60$ kpc bins along coordinate axes x, y, z. The dye mass in each bin is added and shown in Fig. 4 along the three coordinate axes. Cells with dye mass fraction $\leq 10^{-7}$ are excluded from this calculation due to a small fraction of residual dye spreading because of numerical effects. We define the dye spread, Δ_{dye}, in any direction as the width from the $1^{st} - 99^{th}$ percentile of the initially injected dye mass. Thus, $\Delta_{dye,x}$, $\Delta_{dye,y}$, and $\Delta_{dye,z}$ are the sizes of the cloud of dyed material along the three coordinate axes (as shown in Fig. 4). We try other definitions for the spread-like standard deviations and full width at half-maximum with the spread values reducing $\approx$ tenfold and twofold, respectively. Most of our results and conclusions remain unaffected by the choice of definition of spread. We use Δ_{dye} from 1st to 99th percentile definition everywhere in the paper except Section 3.2 where we use the standard deviation definition, which is more appropriate for diffusion coefficient calculations. The reason for choosing 1st to 99th percentile definition everywhere else is because it probes most of the dye mass, representing the true shape of the dye cloud more accurately.

When discussing the dye spread below, we generally refer to the size of the dyed cloud after 200 Myr of evolution, unless otherwise stated (usually where we study the temporal evolution of dye spread, e.g. Section 3.5). For reference, the eddy turnover time for a 5 kpc region in this simulation is $\sim$ 200 Myr ($l/\sigma_{vel} \sim 5$ kpc/25 km s^{-1}), the CGM dynamical and cooling time scales are typically in the order of magnitude of ~ 1 Gyr, and the free-fall time-scales are a few hundred Myr (Tumlinson et al. 2017; Stern et al. 2019; Hafen et al. 2020). So, 200 Myr should be sufficient to look at turbulent
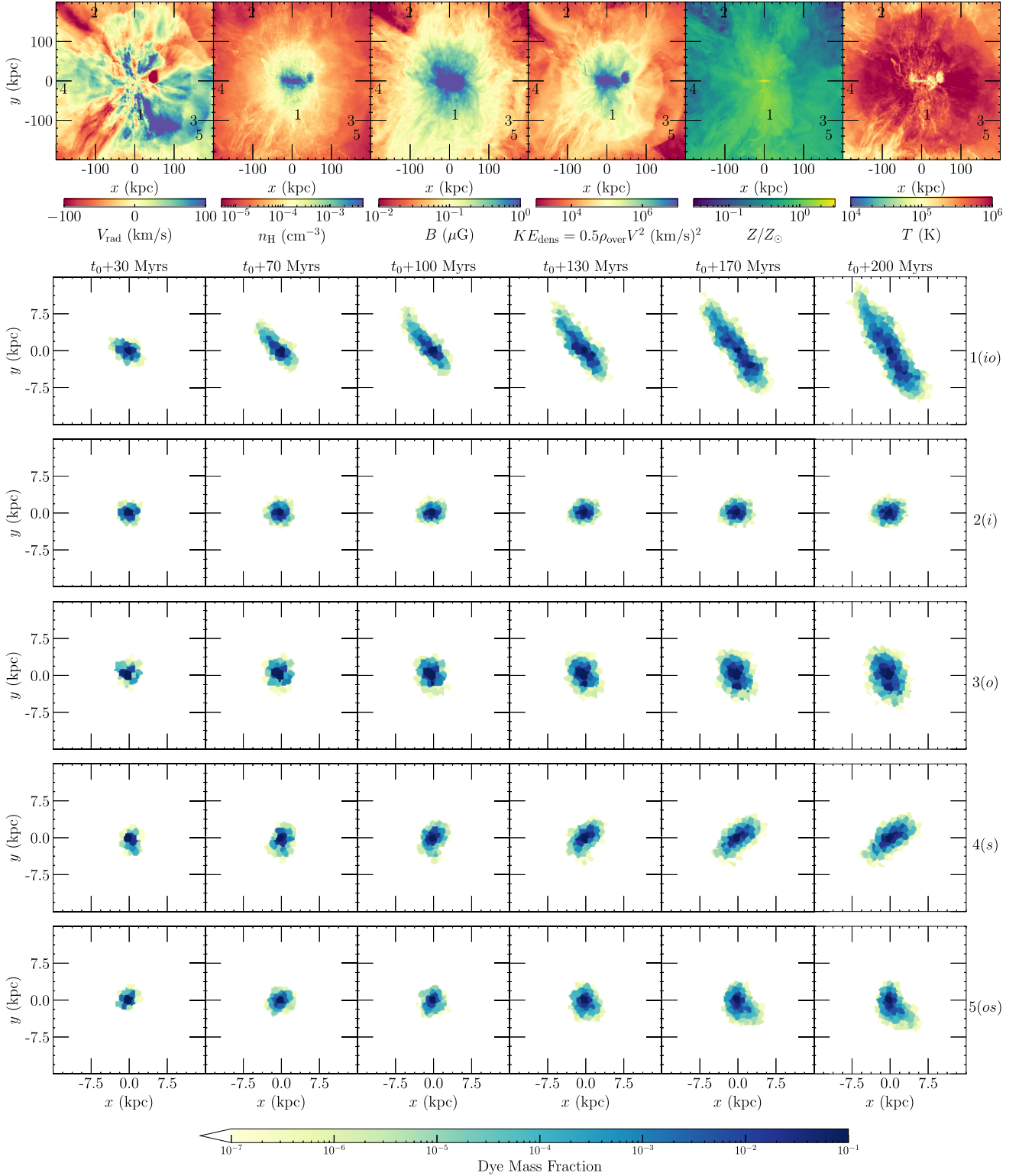
Figure 2. Top panels show edge-on (rotated such that the stellar disc is edge-on) gas projections centred on the main galaxy with 100 kpc depth and 400 kpc × 400 kpc width. From left to right, the panels show the radial velocity, hydrogen number density, magnetic field strength, kinetic energy density, metallicity, and temperature. The five numbers in the top panels show some locations of dye injection. The evolution of dye at the five locations over 200 Myr is shown in the bottom panels in a 40 × 40 kpc box. t_0 is the time the dye was injected into single cells (with a dye mass fraction of 1). Here, the row labelled 1(io) is an outflow from interacting inflows-outflows (io), 2(i) is a pure inflow (i), 3(o) is a pure outflow (o), 4(s) is a pure static flow (s), and 5(os) is an outflow interacting with a static flow (os).
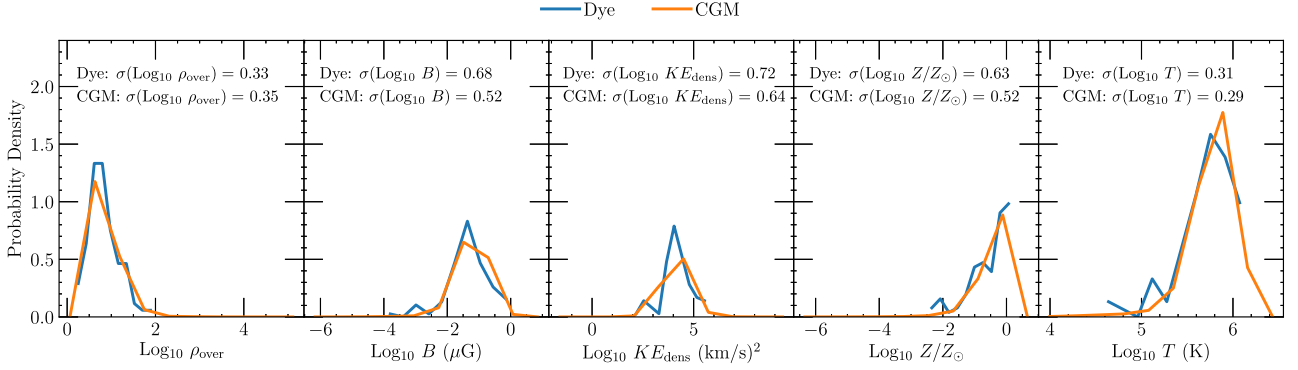
Figure 3. The probability density function of several volume-weighted gas properties of the CGM (orange) and the dye injection cells (blue) with logarithmic binning (bins = 10). The text in every panel shows the standard deviation of the gas property values (in $\log_{10}$) for the dyed cells and the CGM ($50\,\mathrm{kpc} < r < 200\,\mathrm{kpc}$). The standard deviation for the dyed cells is similar to that of the CGM for all gas properties, meaning that the dye selection is from a diverse range of environments that represent the CGM.
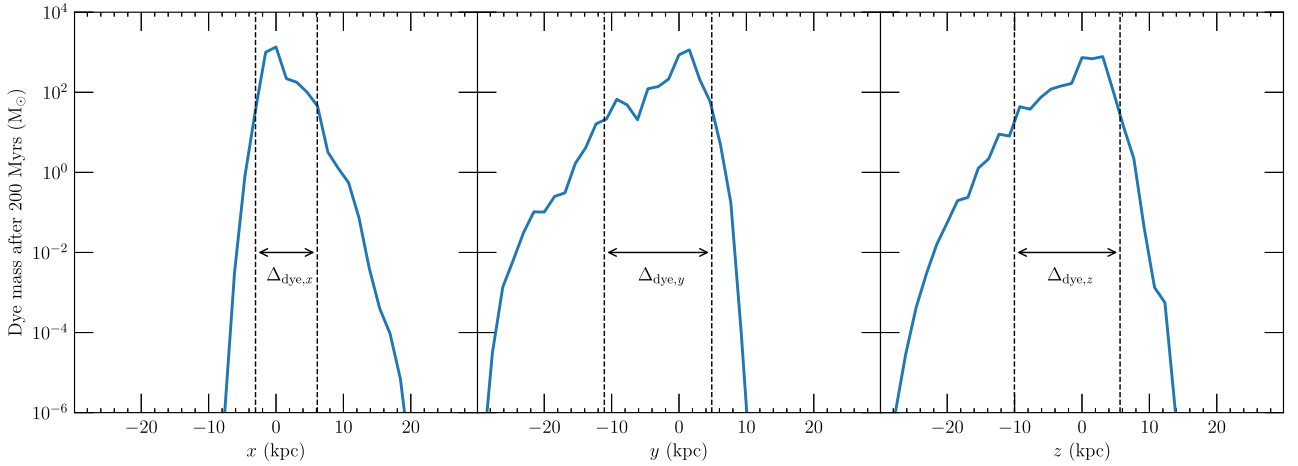
Figure 4. Dye mass 200 Myr after dye injection along the three coordinate axes in a single dye region. The dashed lines represent the 1st and 99th dye mass percentile. The width of the dashed lines ($\Delta_{\mathrm{dye},x}$, $\Delta_{\mathrm{dye},y}$, $\Delta_{\mathrm{dye},z}$) is the dye spread in the x, y, and z directions, respectively.

mixing without the character of the CGM changing significantly. It should be noted that the dye both advects and diffuses. So, we take the cell with the maximum dye fraction as the centre. The resultant moving boxes' average velocity direction is aligned with the bulk velocity direction (averaged over 10 kpc) at the dye injection time. Thus, bulk velocities provide a good estimate for determining the translation/advection of the dye.

3.1 Magnitude of gas mixing

To quantify gas mixing, we use the magnitude of dye spread, i.e. the size of the area containing significant amounts of dye, as $|\Delta_{\mathrm{dye}}| = (\Delta_{\mathrm{dye},x}^2 + \Delta_{\mathrm{dye},y}^2 + \Delta_{\mathrm{dye},z}^2)^{1/2}$. Note that the choice of the axes in the coordinate system is arbitrary and there is no preferential dye spread along any of the coordinate axes. We group dyed regions together that have similar physical properties (see Table 1) and refer to each group as a different 'colour'. First, we explore differences in $|\Delta_{\mathrm{dye}}|$ for different colours corresponding to different flow interactions and physical properties. Since dye spread is caused by the gas mixing with its surroundings, we use the terms gas mixing and dye spread interchangeably from hereon.

Fig. 5 shows the spread averaged over dye regions with similar properties (see Table 1). $|\Delta_{\mathrm{dye}}|$ averaged over different flow interac-

tions (io, i, o, s, os) regardless of their T, KE, or Z is shown as text in Fig. 5. $|\Delta_{\mathrm{dye}}|$ for interacting inflows-outflows (blue, $\langle|\Delta_{\mathrm{dye}}|\rangle_{io}$) is on average (but with large scatter) greater than other flow interactions. The spread for the pure flows (i, o, s) is generally lower than locations with interacting flows (io, os). Since pure flows are more coherent, their motion is relatively ordered on $\mathcal{O}(10\,\mathrm{kpc})$ scales, whereas interacting flows are expected to create more turbulence and have a higher velocity dispersion.

For each flow interaction without the static gas, colour numbers 1, 4, 6, 9, 11, and 13 have a higher $|\Delta_{\mathrm{dye}}|$ than other colours in the corresponding flow interactions. From Table 1, it is clear that these colour numbers correspond to regions with higher kinetic energy. We do not see such a correlation with other selected properties – temperature and metallicity. However, this dependence could be indirect, as gas properties are often correlated in CGM environments. Therefore, we will quantify the correlation between $|\Delta_{\mathrm{dye}}|$ and various local gas properties like temperature, metallicity, density, kinetic energy, and magnetic fields, and derived gas properties like velocity dispersion, and partial derivatives of the velocity field.

Fig. 6 shows (for all 95 selected dye injection locations) the correlation of $|\Delta_{\mathrm{dye}}|$ with several gas properties averaged within the $10 \times 10 \times 10$ kpc region centred on the dye injection location at injection time. Here, kinetic energy density is the volume-specific
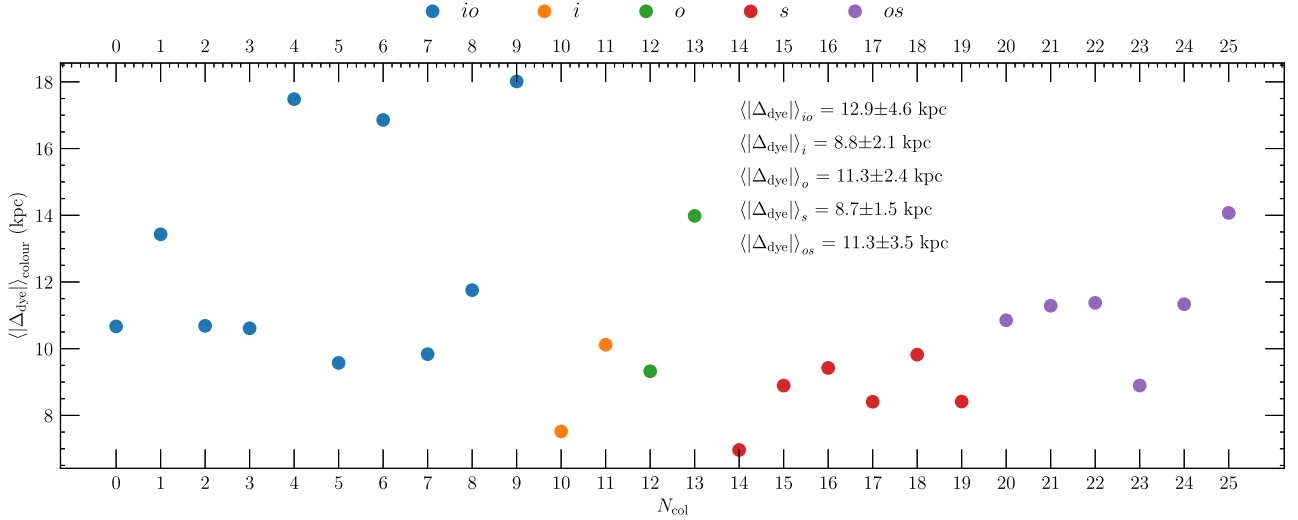
Figure 5. The size of the dyed area after 200 Myr ($|\Delta_{\mathrm{dye}}|$) averaged over injection regions with the same dye colours (see Table 1). Different coloured points in the graph depict different types of gas flow interactions (io, i, o, s, os), and the text inset lists the average of their $|\Delta_{\mathrm{dye}}|$. io are interacting inflow–outflow pairs, i are pure inflows, o are pure outflows, s are pure static flows, and os are outflows interacting with static flows. The inflow–outflow pairs (io) exhibit the highest dye spread, while pure inflows (i) and static flows (s) are among the lowest.

kinetic energy, i.e. $KE_{\mathrm{dens}} = 0.5\rho_{\mathrm{over}}|\vec{V}|^2$, and velocity dispersion (σ_{vel}) is the root mean square of the standard deviation of the velocity vectors ($\vec{V}$). For the local gas properties, we use volume-weighted average temperature (T), metallicity ($Z/Z_\odot$), overdensity (ρ_{over}), and magnetic field (B). The top and middle panels show the correlations of the properties mentioned above. The bottom panel shows the correlations with symmetric ($\mathcal{S}_{ij}$), traceless symmetric ($\mathcal{S}_{ij}^*$), and antisymmetric shear tensors (Ω_{ij}). All of these are derived from the shear tensor,

$$\mathcal{T}_{ij} = \frac{\partial V_i}{\partial x_j}, \tag{1}$$

made up of the partial derivatives of the velocity field. The symmetric part of this tensor $\mathcal{T}_{ij}$ is

$$\mathcal{S}_{ij} = \frac{1}{2}(\mathcal{T}_{ij} + \mathcal{T}_{ji}), \tag{2}$$

the traceless symmetric part of the tensor $\mathcal{T}_{ij}$ is

$$\mathcal{S}_{ij}^* = \frac{1}{2}(\mathcal{T}_{ij} + \mathcal{T}_{ji}) - \frac{1}{3}\delta_{ij}\mathcal{T}_{kk}, \tag{3}$$

where δ_{ij} is the Kronecker delta tensor. The antisymmetric part of the shear tensor is

$$\Omega_{ij} = \frac{1}{2}(\mathcal{T}_{ij} - \mathcal{T}_{ji}). \tag{4}$$

While $\mathcal{S}_{ij}$ represents the strain rate (deformation) of the fluid, its traceless component $\mathcal{S}_{ij}^*$ represents pure shear deformation without any volume change. Ω_{ij} captures the local rigid-body rotation (vorticity) of the fluid. Note that we will often explore the correlations with three tensors, i.e. symmetric shear tensor $\mathcal{S}_{ij}$, traceless symmetric shear tensor $\mathcal{S}_{ij}^*$, and antisymmetric shear tensor Ω_{ij}. Thus, the term 'tensor quantities' in subsequent parts of the study refers to these three tensors in general, and the term 'velocity-derived' quantities refers to σ_{vel} and the tensor quantities (check Beattie et al. 2025, for an overview of the tensors).

To quantify the correlation of dye spread with gas properties, we perform the Spearman rank correlation test, which determines the strength and direction of the monotonic relationship between any two real variables. The Spearman coefficient (r_s) varies between -1 and 1, where -1 indicates a strong negative relationship, 0 indicates no relationship, and 1 indicates a strong positive relationship. All the p-values (mentioned in the caption of Fig. 6) for the null hypothesis that the data sets in are uncorrelated are $< 10^{-5}$, except for temperature (~ 0.05), which only shows a weak correlation. Fig. 6 shows r_s values above each panel; there is some correlation between dye spread and the magnitudes of all the gas properties.[4] Some (such as overdensity, kinetic energy density, velocity dispersion, and tensor quantities) have reasonably high r_s values ≥ 0.5. This multivariate dependence is because CGM properties depend on one another. Table 2 shows the results of the Spearman rank correlation test between gas properties, some of which have high r_s values of ≥ 0.6. In the CGM, properties like ρ decrease radially due to gravity-dominated structure formation, but B, and Z decrease because they are enhanced in the central galaxy and then distributed by feedback (Voort et al. 2021). Additionally, compressing the gas will increase its density and B, while expanding will do the opposite. Velocity dispersion (σ_{vel}) is usually high where CGM flows interact at high velocities, leading to high KE. Thus, these interdependencies could lead to a correlation of dye spread with other gas properties without causation, which makes it difficult to pinpoint the cause of gas mixing in the CGM.

It can be seen from Fig. 6 that out of all selected gas properties, velocity dispersion and symmetric shear tensor magnitudes have the highest Spearman coefficient r_s when correlating with dye spread. This suggests that velocities are a critical factor in determining the rate of gas mixing. The strong dependence of velocity dispersion on other gas properties, as indicated by the high correlation coefficients in Table 2, could explain the high r_s values obtained for KE_{dens} and ρ. Since more ordered flows (i, o, s) have a lower velocity dispersion, they mix less (or more slowly) with their surroundings. This is consistent with our findings in Fig. 5. Naturally, the tensor quantities created from partial derivatives of the velocity fields correlate with

---

[4]The magnitude of any tensor $\mathcal{T}_{ij}$ is derived as $|\mathcal{T}_{ij}| = (2\mathcal{T}_{ij} * \mathcal{T}_{ij})^{1/2}$, also known as the 'Frobenius norm' of a matrix (same as Piomelli & Liu 1995), and is coordinate independent.
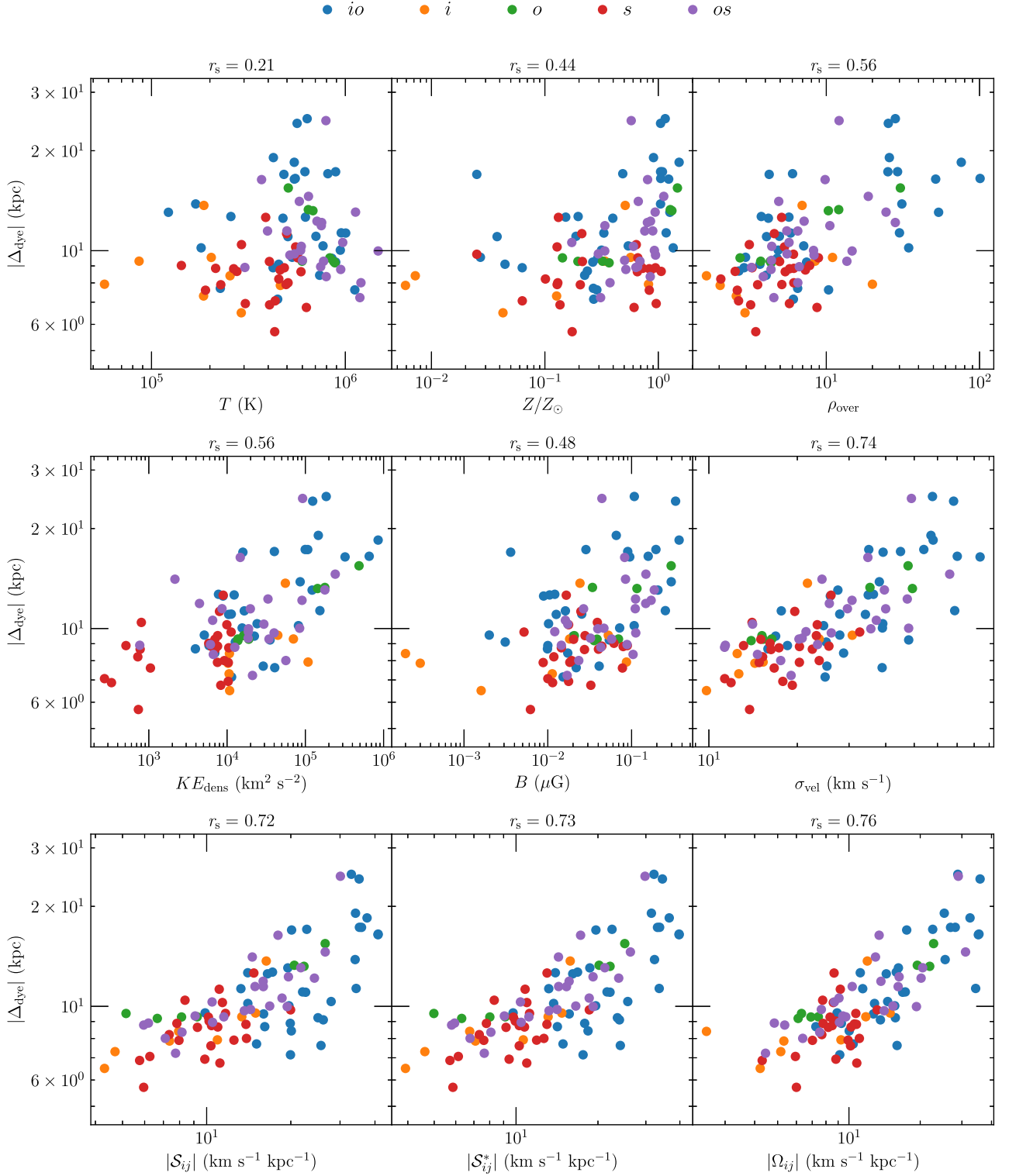
Figure 6. The magnitude of dye spread after 200 Myr as a function of different gas properties averaged in a 10 kpc region around the dye injection locations at injection time. The Spearman rank correlation coefficient (r_s) is shown in the panel titles. From left to right, the top panels show tracer spread correlations with temperature, metallicity, and overdensity, the middle panels show correlations with kinetic energy density, magnetic field, and velocity dispersion, and the bottom panels show the correlations with symmetric, traceless symmetric, and antisymmetric parts of the shear tensor (see equation 1). Both velocity dispersion and tensor quantities correlate strongly with dye spread. The kinetic energy density (KE_{dens}) and overdensity (ρ_{over}) also show a significant correlation, possibly due to their dependence on σ_{vel} (see Table 2). P-values for gas properties from left to right in the top panel are 4.4×10^{-2}, 8.7×10^{-6}, 4×10^{-9}; in the middle panel, 3.3×10^{-9}, 1×10^{-6}, 1.3×10^{-17}; and in the bottom panel, 4.1×10^{-16}, 5.1×10^{-17}, and 3.1×10^{-19}.

Table 2. This table shows the Spearman rank coefficient (r_s, to quantify correlation strength) between some averaged gas properties of the selected regions ($10 \times 10 \times 10$ kpc boxes). Results show significant correlations ($r_s \geq 0.6$) between σ_{vel} and ρ_{over}, KE_{dens}, $|\mathcal{S}_{ij}|$, and $|\Omega_{ij}|$.

Properties	r_s
σ_{vel} versus T	0.28
σ_{vel} versus $Z/Z_{\odot}$	0.42
σ_{vel} versus ρ_{over}	0.69
σ_{vel} versus KE_{dens}	0.63
σ_{vel} versus B	0.48
σ_{vel} versus $|\mathcal{S}_{ij}^*|$	0.91
σ_{vel} versus $|\Omega_{ij}|$	0.91

velocity dispersion as well. In fact, SPH codes often use σ_{vel} or $|\mathcal{S}_{ij}^*|$ for subgrid-scale models of turbulent mixing (Wadsley et al. 2008; Williamson et al. 2016). The latter comes from the Smagorinsky equation, which can be expressed as

$$D = (C_s h)^2 |\mathcal{S}_{ij}^*|, \tag{5}$$

where D is the Smagorinsky diffusivity, C_s is the Smagorinsky model constant, and h is the resolution scale.

To fully understand the relationship between properties with higher r_s and gas mixing and to identify other factors that may influence this process, we explore the spatial and temporal relationships of σ_{vel}, KE_{dens}, ρ, and tensor quantities at different times after dye injection with $|\Delta_{\text{dye}}|$ 200 Myr after dye injection in Fig. 7. Five different analysis box sizes (5, 10, 15, 20, 25 kpc) are selected at all output times (from t_0, dye injection time, to $t_0 + 200$ Myr, in 10 Myr spacing) to a create a region around the 95 dye injected cells (where the box centre follows the cell with highest dye mass as the simulation evolves). Gas properties averaged in each analysis region are correlated with $|\Delta_{\text{dye}}|$ at $t_0 + 200$ Myr at every output time. The tensor quantity plots (right panels) contain the calculation performed at the dye centre as well, since the tensor quantities can be accurately computed there without the need for averaging. The r_s values are plotted in Fig. 7. The error bars represent 1σ confidence levels from bootstrapping the r_s samples 10^4 times.

The r_s values change significantly with time and box size for σ_{vel} and symmetric tensor quantities while remaining nearly constant for KE_{dens} and ρ. The changes in the values of σ_{vel} are marginal with time and scale up with increasing box sizes (see Fig. B1 in Section B) because larger boxes usually probe more of the random motions in the CGM. The presence of laminar shearing flows could also increase the velocity dispersion; however, the systematic increase of σ_{vel} with the box sizes suggests that laminar shearing flows are possibly in all directions, becoming more equivalent to turbulent motions. Since the magnitudes of quantities do not affect Spearman rank correlation test results, scaled-up σ_{vel} values for different box sizes also should not affect r_s. However, the correlation of Δ_{dye} at $t_0 + 200$ Myr with these σ_{vel} samples changes significantly. On the other hand, the evolution of KE_{dens} and ρ_{over} is significant (the standard deviation increases by a factor of 2 over 200 Myr, see Fig. B1). Despite that, their correlation with Δ_{dye} does not vary significantly (within 1σ error). These results suggest that the correlation between dye spread and σ_{vel} is stronger and more sensitive to variations than the correlation between dye spread and KE_{dens} and ρ. When applying the same arguments to the tensor quantities, we find that the dye spread correlates best with the symmetric parts. The traceless symmetric part exhibits very similar behaviour to just the symmetric part, suggesting that pure shear, rather than volumetric expansion/contraction, drives gas mixing,

as expected. The correlation with the antisymmetric tensor is also strong, possibly due to its correlation with the σ_{vel} (see Table 2). Thus, the high r_s values (maximum ~ 0.87) indicate a strong dependence of Δ_{dye}, and hence of gas mixing, on the velocity dispersion and the shear of the surrounding medium.

As we increase the analysis box size, the overall r_s at all times reduces significantly in the case of σ_{vel} and the tensor quantities (see top-left and right panels of Fig. 7), suggesting a stronger dependence of Δ_{dye} (average Δ_{dye} for all dyes after 200 Myr is ≈ 11 kpc) on smaller regions surrounding the dyed areas. Velocity-derived quantities are the primary cause of the dye mixing. Since larger boxes are more likely to have regions without dye, their velocity dispersion and average tensor quantities (tensor magnitudes averaged over the region) would include undyed regions, causing the correlation with Δ_{dye} to worsen. Additionally, the smaller boxes contain highly concentrated dye (see Fig. 2), so their velocity-derived quantities also cause a larger change in dye spread compared to more diluted areas of the dye. Thus, the extent of the mixed gas ($|\Delta_{\text{dye}}|$) is best predicted with σ_{vel} and the symmetric shear tensors (see equation 5) in smaller regions around the dye.

We can draw more inferences from the time evolution of r_s with σ_{vel} and symmetric shear tensors. For the smaller regions, a maximum always occurs between $\approx t_0 + 70$ Myr and $t_0 + 120$ Myr, implying that the mixing of gas from a cell with its surroundings after 200 Myr is best defined by the velocity-derived quantities between $t_0 + (70 - 120)$ Myr. This suggests a delay in the transfer of the local velocity dispersion and shear to the spread of the dye. Because, if it were instantaneous, a continuous rise in r_s would be expected. The initial increase in r_s could be due to the dye gradually filling the box where the velocity-derived quantities are calculated, such that their transfer to the dye spread becomes more optimal. When we perform the same simulations with dye injection in $2 \times 2 \times 2$ kpc clumps (a collection of 8 cells around the original dye injection cells) instead of 1 kpc cells, the results remain qualitatively the same (see Fig. B2 in Section B). However, the location of the maximum shifts slightly towards earlier times, between $t_0 = 50$ and 100 Myr, perhaps due to the dye injected in clumps covering the box more quickly, thus reaching an optimal configuration for the transfer of σ_{vel} and shear to dye spread sooner.

3.2 Diffusion coefficient

With our tracer dyes, we can calculate the average diffusion coefficient over T (Myr) as

$$\langle \text{DC} \rangle_T = |\Delta_{\text{dye}}|^2 \, T \text{ (Myr)}, \tag{6}$$

where we substitute $T = 200$ Myr, the time-scale over which we track the dye. We use the standard deviation of dye spread Δ_{dye} throughout this section, as it aligns with the physics of diffusion and focuses on the bulk of the dye distribution rather than the tails. The resulting diffusion coefficients are shown in the top panel of Fig. 8. Assuming a power-law dependence of the diffusion coefficient on the velocity dispersion, we determine the power-law exponent to be $n \approx 1.1$ (almost linear).[5]

We then correlate this diffusion coefficient with the velocity dispersion and symmetric shear tensors (based on results from Section 3.1). SPH codes also use similar models for diffusivity in their subgrid models (Klessen & Lin 2003; Wadsley et al. 2008; Greif et al. 2009; Shen et al. 2013; Williamson et al. 2016; Colbrook et al.

---

[5]We find similar power-law exponents, $n \sim 1.1$, for simulations with standard + 2 kpc refinement.
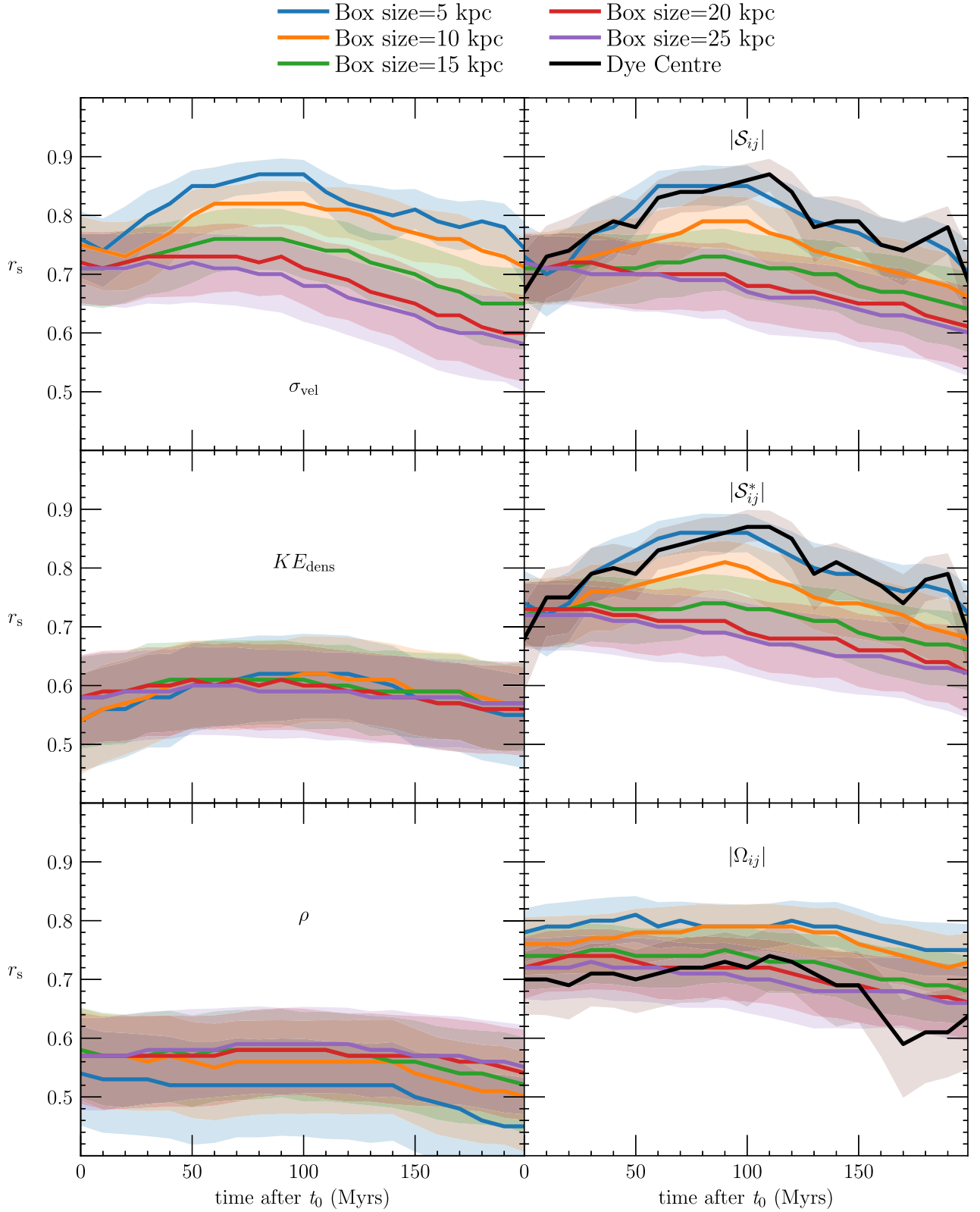
Figure 7. Spearman rank coefficient (r_s) of the correlation between the magnitude of dye spread after 200 Myr and averaged gas properties in differently sized boxes (see legend) around the injected dye at each simulation output time. The error bars represent 1σ confidence intervals from bootstrapping the sample 10^4 times. Among the six gas properties shown, $\sigma_{\rm vel}$, $|\mathcal{S}_{ij}|$, and $|\mathcal{S}_{ij}^*|$ provide the highest $r_s \sim 0.86$. The maximum correlation for $\sigma_{\rm vel}$ and the tensor quantities occurs in a 5 kpc box, and at the dye centre, respectively, at ~ 100 Myr. Other properties produce lower r_s values and marginal changes with time and box size, suggesting an indirect correlation.
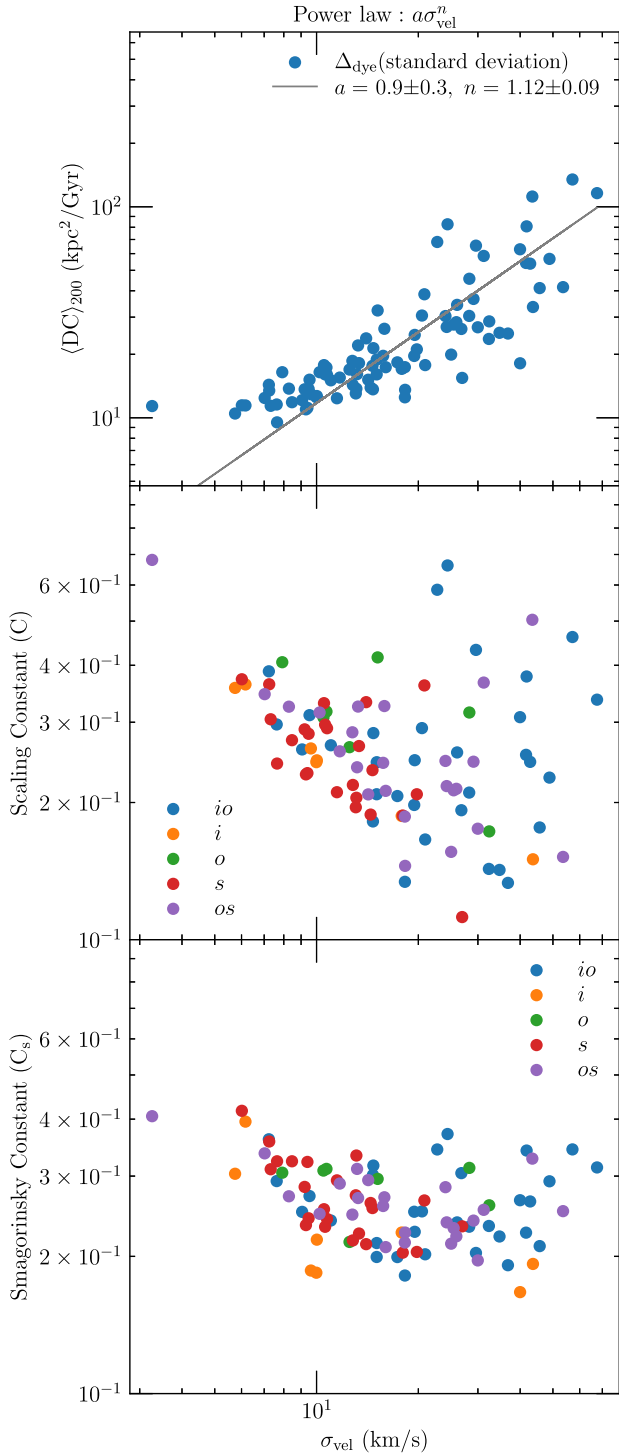
Figure 8. The top panel shows the average diffusion coefficients for dyes over 200 Myr, calculated as $|\Delta_{\mathrm{dye}}|^2/(200\,\mathrm{Myr})$, as a function of velocity dispersion. The standard deviation definition of Δ_{dye} is used. Black lines show a power-law fit (parameters mentioned in the title and legend). The diffusion coefficients scale almost linearly ($n = 1.1 \pm 0.09$) with the velocity dispersion. The middle and bottom panels show the scaling constant (C, computed using equation 7) and Smagorinsky constant (C_s, computed from equation 8), respectively. We derive these constants for our simulations using well-known subgrid diffusion coefficient estimation methods of SPH simulations. We find a good agreement between typical values in the literature and our values (both are approximately C = 0.1–1 and C_s = 0.2–0.4).

2017; Rennehan et al. 2019; Rennehan 2021). Some studies estimate that the diffusion coefficient $= C\,\sigma_{\mathrm{vel}}\,l_{\mathrm{turb}}$, where C is the scaling constant (usually assumed to vary from 0.1 to 1, as seen in Wadsley et al. 2008), and l_{turb} is turbulent scale relevant for gas mixing (they assume it to be equal to the simulation resolution). Given that the dye spread allows us to calculate the actual diffusion coefficient in our simulations (equation 6), we can estimate the scaling constant C from the SPH definition for our simulation as

$$C = |\Delta_{\mathrm{dye}}|^2/(200\,\mathrm{Myr}\,\sigma_{\mathrm{vel}}\,l_{\mathrm{turb}}), \qquad (7)$$

where C (scaling constant) is a factor that scales the estimated diffusion coefficient ($\sigma_{\mathrm{vel}}\,l_{\mathrm{turb}}$) to the actual diffusion coefficient (equation 6), l_{turb} is the approximate average length-scale of dye evolution over 200 Myr (5 kpc), and σ_{vel} is the velocity dispersion around our dyes at l_{turb} scales. Because $|\Delta_{\mathrm{dye}}|$ after 200 Myr correlates the best with velocity dispersion in regions of 5 kpc (see Fig. 7), it is a reasonable to assume $l_{\mathrm{turb}} = 5$ kpc. It should be noted that turbulence can often be driven on much larger-scales (a few tens to hundreds of kpc) in the CGM (see fig. 8 in Pakmor et al. 2020). However, the turbulent length-scales responsible for dye mixing are smaller than or similar to the extent of dye spread, cascaded down from large-scale turbulence.

Similar to the scaling constant derivation above, we can determine the Smagorinsky constant C_s by estimating the diffusivity from the Smagorinsky equation (equation 5). In this case,

$$C_d s^2 = |\Delta_{\mathrm{dye}}|^2/(200\,\mathrm{Myr}\,|\mathcal{S}_{ij}^*|\,l_{\mathrm{turb}}^2), \qquad (8)$$

where we replace the resolution scale h with the approximate turbulent length-scale over 200 Myr ($l_{\mathrm{turb}} = 5$ kpc). The middle and bottom panels of Fig. 8 show the scaling constant C and Smagorinsky constant C_s for our simulation, respectively, for different flow types. C ranges 0.09–0.7, similar to scaling constants used in subgrid models in SPH simulations, ranging from 0.1 to 1 (Williamson et al. 2016). C_s in our simulation ranges from 0.2 to 0.4 (see bottom panel of Fig. 8). These values are similar to those found in the literature – $C_s = 0.2$ (Clark, Ferziger & Reynolds 1979), $C_s = 0.1$–0.2 (Garnier et al. 2009), $C_s = 0.37$ (Shen et al. 2010, 2013; Brook et al. 2014), and $C_s = 0.29$ (Wadsley, Keller & Quinn 2017).[6] Moreover, we do not see any dependency of these constants on different flow types.

Obtaining constants C and C_s similar to the values in the literature is promising for both the implicit model of mixing in our simulation and the typical subgrid models used in certain SPH simulations. However, the implications require careful consideration. The diffusion coefficient of the dye is a time-varying quantity for our simulations. As the dye evolves, the relevant σ_{vel} and l_{turb} for estimating the diffusion coefficient also change. Since we do not account for this in this section, reported scaling constants are approximately the average scaling constants for gas mixing over 200 Myr (which are for a time-step in subgrid mixing models). In addition, numerical mixing is present in our simulations (see Section 3.5). Thus, more detailed time-dependent analysis at different resolutions is required to disentangle these factors, which is beyond the scope of this study.

3.3 Direction of gas mixing

In the previous subsection, we discussed the dependence of the magnitude of gas mixing on physical properties. Here, we analyse the di-

---

[6]Note that there are many different definitions of the Smagorinsky constant in the literature; Rennehan et al. (2019) performed the correct conversions of other definitions to the C_s we use.

rectional dependence of gas mixing on physical properties. To do this, we correlate the spread vector ($\vec{\Delta}_{\text{dye}} = \Delta_{\text{dye},x}\hat{i} + \Delta_{\text{dye},y}\hat{j} + \Delta_{\text{dye},z}\hat{k}$) with several physical property vectors – velocity dispersion ($\vec{\sigma}_{\text{vel}} = \sigma_{V_x}\hat{i} + \sigma_{V_y}\hat{j} + \sigma_{V_z}\hat{k}$), $\vec{V}$, $\vec{B}$, and magnetic field dispersion computed from standard deviations of magnetic field vector components ($\vec{\sigma}_B = \sigma_{B_x}\hat{i} + \sigma_{B_y}\hat{j} + \sigma_{B_z}\hat{k}$). To compare with the tensor quantities, we use combinations of tensor eigenvalues and eigenvectors to create vectors with physical meanings. Since quantities derived from symmetric and traceless symmetric tensors yield similar results, we only show results from the latter. For the traceless symmetric ($\mathcal{S}_{ij}^*$) shear tensor, we construct three vectors each as follows:

$$\vec{\mathcal{S}}_{ij,\text{min}}^* = \lambda_{\text{min}}\vec{E}_{\text{min}}, \tag{9}$$

$$\vec{\mathcal{S}}_{ij,\text{max}}^* = \lambda_{\text{max}}\vec{E}_{\text{max}}, \tag{10}$$

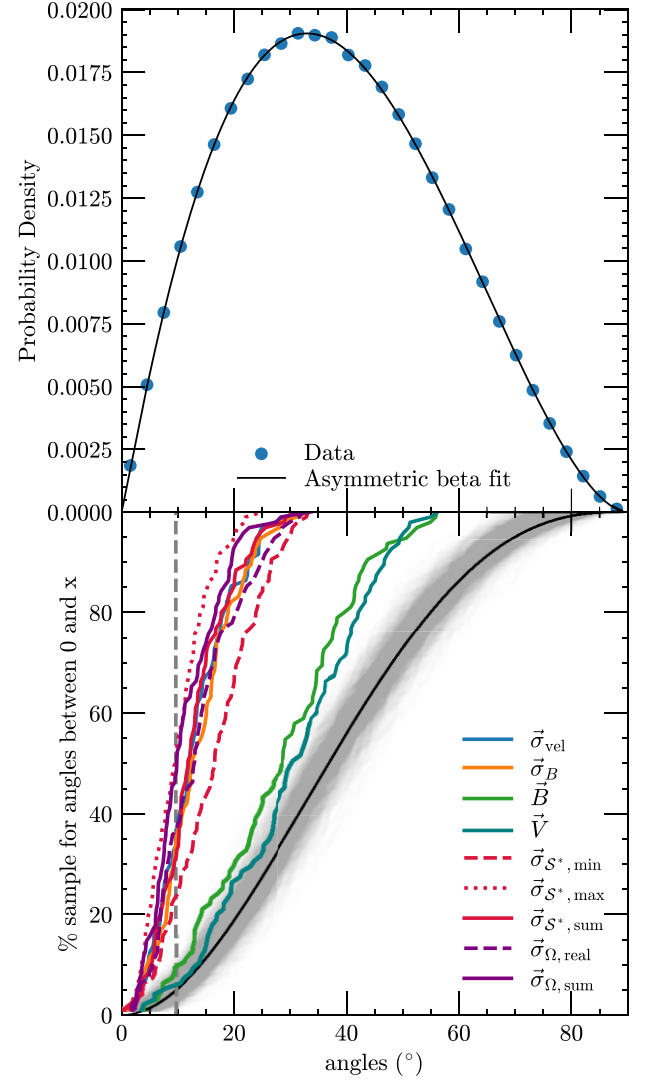$$\vec{\mathcal{S}}_{ij,\text{sum}}^* = \Sigma_n \lambda_n \vec{E}_n. \tag{11}$$

Here, λ and $\vec{E}$ represent n eigenvalues and the corresponding unit eigenvectors of symmetric tensors, respectively. $\lambda_{\text{min/max}}$ and $\vec{E}_{\text{min/max}}$ are the minimum/maximum eigenvalues and the corresponding eigenvectors, respectively. The symmetric shear tensors always have three real eigenvalues with at least one positive and one negative value. Importantly, the positive and negative eigenvalues represent the strengths of deformation, either stretching or compression, without any volume change, respectively. The corresponding eigenvectors point in the directions of stretching and compression. Note that deformation (changes in shape) is distinct from volumetric changes (expansion or contraction) in the fluid. Since both symmetric and traceless symmetric shear tensors yield similar results, we argue that volumetric changes, compared to deformation, play a minimal role in mixing the dyes in our simulations. Similarly, for antisymmetric shear tensors, we create two vectors as follows:

$$\vec{\Omega}_{ij,\text{real}} = \lambda_{\text{real}}\vec{E}_{\text{real}}, \tag{12}$$

$$\vec{\Omega}_{ij,\text{sum}} = \Sigma_n \lambda_n \vec{E}_n. \tag{13}$$

Since the antisymmetric shear tensor has one real eigenvalue λ_{real} (~ 0), we use it with the corresponding eigenvector $\vec{E}_{\text{real}}$ to create $\vec{\Omega}_{ij,\text{real}}$, which points towards the rotational axis. The imaginary eigenvalues of a real antisymmetric matrix are complex conjugates, and their corresponding eigenvectors are also complex conjugates (representing the plane of rotation); therefore, the vector created by the sum of all the eigenvalues and eigenvectors $\vec{\Omega}_{ij,\text{sum}}$ is also real. Since $\lambda_{\text{real}} \sim 0$, the summation leads to $\vec{\Omega}_{ij,\text{sum}}$ pointing in the direction perpendicular to the rotational axis, i.e. the plane of rotation. Similar to the calculation of the velocity and magnetic field dispersion in boxes, we take the standard deviation of the three components of the vectors constructed above from tensors, and show the resultant vectors as $\vec{\sigma}_{\mathcal{S}^*,\text{min}}$, $\vec{\sigma}_{\mathcal{S}^*,\text{max}}$, $\vec{\sigma}_{\mathcal{S}^*,\text{sum}}$, $\vec{\sigma}_{\Omega,\text{real}}$, and $\vec{\sigma}_{\Omega,\text{sum}}$.

We now have vectors for all the quantities of interest. Typically, vectors can point in any direction; however, all the vectors we construct only have positive components[7]; thus, they point in a single positive octant. Then we compute the angle between $\vec{\Delta}_{\text{dye}}$ and these positive component vectors. The distribution of angles between random positive vectors is different from full 3D vectors. Thus, we generate a control sample by calculating angles between two random vectors, distributed uniformly in spherical geometry, free to point anywhere in one octant (with all positive values). The top

---

[7]If the vectors do not have positive components, as in the case of $\vec{B}$ and $\vec{V}$, we take the absolute values of their components for this analysis.

Figure 9. The top panel shows the PDF of possible angles between two random vectors in the positive 3D octant. The black curve shows an asymmetric beta function fit (for smoothing) to blue data points (generated using 10^5 uniformly-spaced random vector pairs). The bottom panel shows the cumulative distribution functions (CDF) as percentages corresponding to alignments within x-axis angles. The black curves are the control sample CDFs, created from the top panel fit to the PDF. The coloured curves in the bottom panel correspond to angles between $\vec{\Delta}_{\text{dye}}$ and gas properties $\vec{\sigma}_{\text{vel}}$, $\vec{\sigma}_B$, $\vec{B}$, $\vec{V}$, $\vec{\sigma}_{\mathcal{S}^*,\text{min}}$, $\vec{\sigma}_{\mathcal{S}^*,\text{max}}$, $\vec{\sigma}_{\mathcal{S}^*,\text{sum}}$, and $\vec{\sigma}_{\Omega,\text{real}}$. 5 per cent of the random vectors lie within 9.6 deg of one another, as shown by the grey dashed line. All the selected gas properties exhibit a higher directional correlation with $\vec{\Delta}_{\text{dye}}$ than the random control sample.

panel of Fig. 9 shows the probability density of the angles between pairs of these random vectors ($\theta = [0, \pi/2]$). The data is fitted to an asymmetric beta function

$$f(x; \alpha, \beta_b, k) = \frac{x^\alpha (90-x)^{\beta_b} \exp(-kx)}{90^{\alpha+\beta_b+1} B(\alpha+1, \beta_b+1)}, \tag{14}$$

where

$$B(a, b) = \int_0^1 t^{a-1}(1-t)^{b-1}\,\mathrm{d}t, \tag{15}$$

Table 3. This table shows the mean angle and its standard deviation between dye spread and the physical properties $\vec{\sigma}_{\mathrm{vel}}$, $\vec{\sigma}_B$, $\vec{V}$, $\vec{B}$, $\vec{\sigma}_{\mathcal{S}^*,\mathrm{min}}$, $\vec{\sigma}_{\mathcal{S}^*,\mathrm{max}}$, $\vec{\sigma}_{\mathcal{S}^*,\mathrm{sum}}$, $\vec{\sigma}_{\Omega,\mathrm{real}}$, $\vec{\sigma}_{\Omega,\mathrm{sum}}$, as well as the control sample.

Properties	Angle (°)
$\vec{\sigma}_{\mathrm{vel}}$	12.96 ± 3.35
$\vec{\sigma}_B$	13.62 ± 3.42
$\vec{V}$	30.43 ± 6.39
$\vec{B}$	28.19 ± 6.49
$\vec{\sigma}_{\mathcal{S}^*,\mathrm{min}}$	16.56 ± 3.9
$\vec{\sigma}_{\mathcal{S}^*,\mathrm{max}}$	9.96 ± 2.63
$\vec{\sigma}_{\mathcal{S}^*,\mathrm{sum}}$	12.77 ± 3.21
$\vec{\sigma}_{\Omega,\mathrm{real}}$	13.69 ± 3.68
$\vec{\sigma}_{\Omega,\mathrm{sum}}$	11.22 ± 3.14
Control sample	37.90 ± 9.20

is the beta function. The best-fitting parameters are $\alpha = 1.04$, $\beta_b = 1.80$ and $k = 1.7 \times 10^{-5}$. The fitting is done to remove the statistical variations due to a finite number of data points. This control sample represents the distribution in a set of random uncorrelated positive vectors and can be compared to the distribution of angles between $\vec{\Delta}_{\mathrm{dye}}$ and vectors representing physical properties of the gas.

The bottom panel of Fig. 9 shows the cumulative distribution functions (CDF) (as percentages) of the above control sample PDF (solid black curve) and the angles between $\vec{\Delta}_{\mathrm{dye}}$ and $\vec{\sigma}_{\mathrm{vel}}$, $\vec{\sigma}_B$, $\vec{B}$, $\vec{V}$, $\vec{\sigma}_{\mathcal{S}^*,\mathrm{min}}$, $\vec{\sigma}_{\mathcal{S}^*,\mathrm{max}}$, $\vec{\sigma}_{\mathcal{S}^*,\mathrm{sum}}$, and $\vec{\sigma}_{\Omega,\mathrm{real}}$. The grey shaded region in the bottom panel represents 1000 different CDFs with 95 random data points (equal to the number of dyes) from the control sample to showcase statistical variations due to a limited number of available data points. All vectors are computed at the dye injection time in a 10 kpc box around the injection location 100 Myr after injection, and $\vec{\Delta}_{\mathrm{dye}}$ is calculated 200 Myr after dye injection. The physical property CDFs are created from the 95 dye injection locations.

Compared to the control sample, all properties have more alignment with $\vec{\Delta}_{\mathrm{dye}}$ as they have higher CDFs. In Table 3, we quantify the average angle between dye spread and physical properties. All the average angles are smaller than the control sample average angle, with $\vec{\sigma}_{\mathcal{S}^*,\mathrm{max}}$ exhibiting the highest alignment. This suggests that the dyed cloud's shape is determined by the dispersion of stretching eigenvectors. Put simply, the direction with the greatest variance in fluid stretching deformation is where the most gas mixing occurs. The high angular alignment of the dye spread with $\vec{\sigma}_B$ and $\vec{\sigma}_{\mathrm{vel}}$ suggests that magnetic fields and velocity fields are also aligned within themselves (Seta et al. 2020; Seta & Federrath 2021). When we performed the same experiment with the positive components of the averages of these vectors rather than the standard deviation (see $\vec{B}$ and $\vec{V}$ in Fig. 9), we found that the level of alignment is closer to the control sample, suggesting that dispersion is a better measure of the diffusive processes. It is difficult to pinpoint the best aligning physical quantity by analysing just one region size and time; thus, we perform the spatial and temporal analysis in the same way as Fig. 7 for some of the best aligning vectors from Fig. 9.

Fig. 10 shows the percentage of the sample for angles lower than $9.6°$ (corresponding to 5 per cent of the control sample, shown as grey dashed lines in Figs 9 and 10) between $\vec{\Delta}_{\mathrm{dye}}$ and $\vec{\sigma}_{\mathrm{vel}}$ (top-left panel), $\vec{\sigma}_B$ (top-right panel), $\vec{\sigma}_{\mathcal{S}^*,\mathrm{max}}$ (bottom-left panel), and $\vec{\sigma}_{\Omega,\mathrm{sum}}$ (bottom-right panel). This is computed for $\vec{\Delta}_{\mathrm{dye}}$ after 200 Myr for physical properties inside differently sized analysis boxes at every simulation output time. Every quantity shows a clear alignment with dye spread, regardless of box size or time and this result does not qualitatively depend on our choice of $9.6°$. Generally, smaller boxes show a weaker correlation than larger boxes. Moreover, a higher per cent of the dyes

(~ 60 per cent) are more aligned (angles $\leq 9.6°$) with $\vec{\sigma}_{\mathcal{S}^*,\mathrm{max}}$ and $\vec{\sigma}_{\Omega,\mathrm{sum}}$ compared to $\vec{\sigma}_{\mathrm{vel}}$ and $\vec{\sigma}_B$ (~ 35 per cent). Thus, the dye shape is best determined by the dispersion of stretching (deformation) and plane of rotation eigenvectors in boxes spanning the dye volume (box size ≥ 10 kpc) unlike dye spread magnitudes which correlated the best with boxes containing high dye mass concentrations (box size ~ 5 kpc). The average dye spread is ~ 11 kpc after 200 Myr. Larger boxes (≥ 10 kpc) correlating better with the dye spread shape suggest that the correlation forms later in the evolution. Since the best correlation for dye spread magnitude is between 70 and 120 Myr after injection (see Fig. 7), the spread shape probably changes faster than the spread magnitude. However, the temporal trend for alignment analysis is statistically insignificant, because variations with time in Fig. 10 are within error bars. Combining the alignment results with our results from Section 3.1 and Fig. 7, we conclude that the traceless symmetric shear tensor best predicts both the magnitude and shape of gas mixing in our simulations.

3.4 Radial profile of gas mixing

As established in the earlier sections, the amount of gas mixing in the CGM of galaxies is heavily influenced by the velocity dispersion of the local surroundings. Fig. 11 shows the velocity dispersion as a function of distance from the galactic centre (r) for three spherical regions, with diameters 5, 10, and 20 kpc. To calculate velocity dispersion at a particular radius, all cells with a radial distance between $r - 0.5$ kpc and $r + 0.5$ kpc are selected. Out of these, 100 bootstrap samples containing 100 random spherical regions are generated. Spheres with a diameter equal to the region size are created around all these cells. The velocity dispersion is calculated by the volume-weighted standard deviation of the velocities of cells in these spheres. The median of 100 random cells is taken for each sample, and the median of 100 samples is reported as the velocity dispersion at that r. The shaded blue region represents the standard deviation of the velocity dispersion values for 5 kpc regions. All cells were used to compute this scatter instead of bootstrapping, making it computationally prohibitive to perform the same calculation for the 10 and 20 kpc regions. The standard deviation for the 10 and 20 kpc regions is expected to scale up the same as their velocity dispersion values.

The velocity dispersion decreases with radius, possibly due to higher gas flow activity happening closer to the centre because of outflows driven by stellar or AGN feedback, gas stripping from satellite galaxies, and higher inflow velocities (Voort et al. 2021). σ_{vel} is also larger for larger regions because large regions sample a more variable environment, as expected for turbulent flows (Larson 1981; Heyer & Brunt 2004; Federrath & Klessen 2012). From Fig. 11, we find the relation $\sigma_{\mathrm{vel}} \propto l_{\mathrm{d}}^{0.4-0.6}$, where l_{d} is the scale length of the region, i.e. the diameter of the region in which σ_{vel} is calculated. The scaling exponent is close to $1/2$, which is the value expected for supersonic turbulence (Kritsuk et al. 2007; Federrath et al. 2010, 2021).

The radial decrease of the velocity dispersion should cause a reduction in the amount of gas mixing in the CGM. Additionally, other properties of the CGM, such as metallicity and magnetic fields, also exhibit decreasing trends radially (see fig. 6 in Voort et al. 2021). Metals and magnetic fields originate primarily from the central galaxy and are ejected outwards in the galactic wind (Christensen et al. 2018). A lot of this material within a few tens of kiloparsecs from the galaxy centre is recycled back to the ISM (Grand et al. 2019). Additionally, the remaining material mixes more with regions closer to the galaxy centre and less with regions
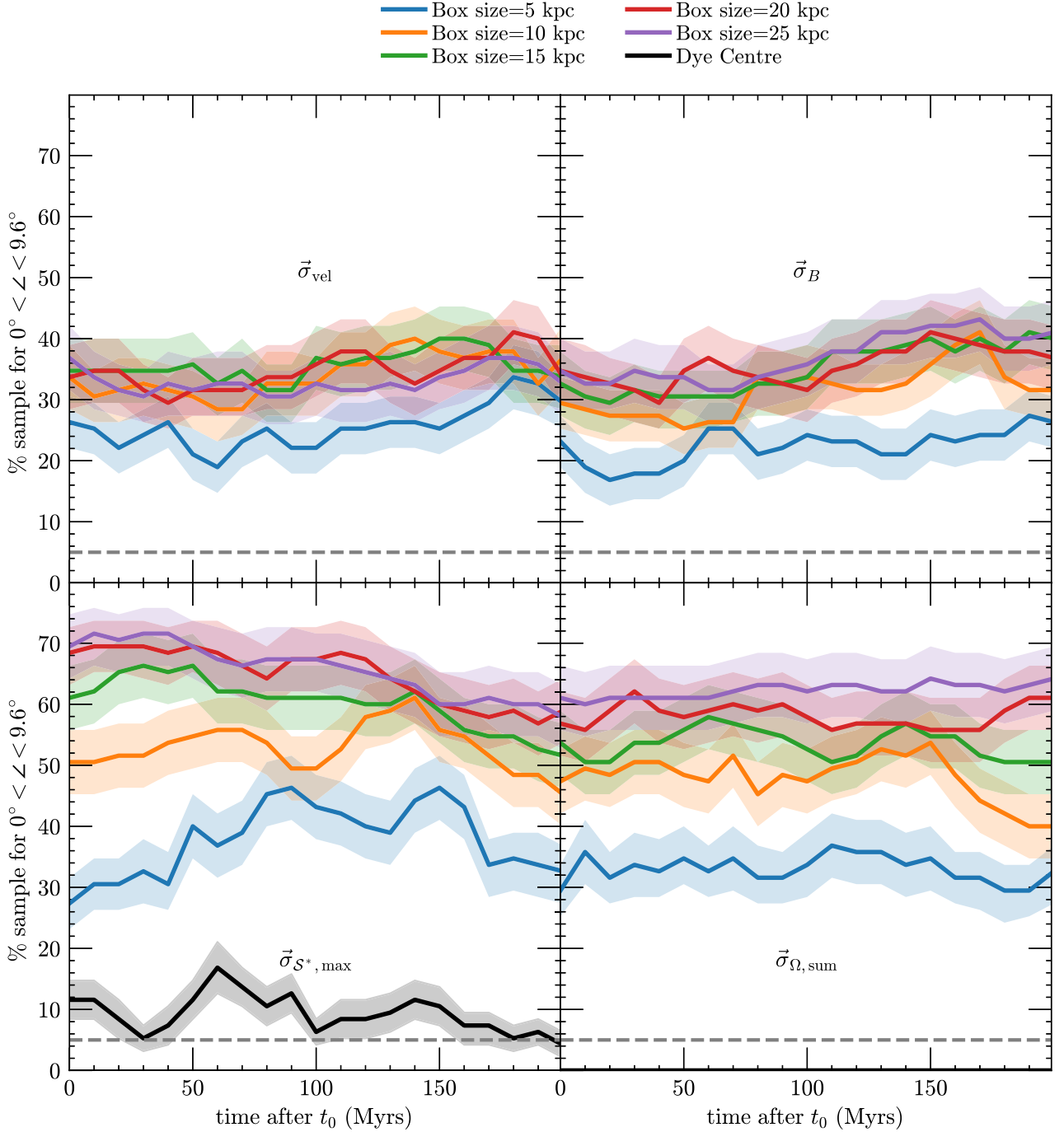
Figure 10. The percentage of dyes, $\vec{\Delta}_{\rm dye}$, with the direction of dye spread (after 200 Myr) aligned within 9.6° of $\vec{\sigma}_{\rm vel}$ (top-left panel), $\vec{\sigma}_B$ (top-right panel), $\vec{\sigma}_{\mathcal{S}^*,\rm max}$ (bottom-left panel), and $\vec{\sigma}_{\Omega,\rm sum}$ (bottom-right panel), computed in different analysis box sizes as per the legend, as a function of time. The grey dashed line (5 per cent) represents the control sample (same as the one in Fig. 9). Larger boxes tend to show stronger alignment than the smallest box (5 kpc). Quantities associated with the dispersion of stretching and plane of rotation eigenvectors exhibit a higher alignment with the dye shape than the dispersion of velocities and magnetic fields.

farther away due to the global velocity dispersion structure (Fig. 11). A combination of these effects could create radially decreasing trends. Additionally, metal diffusion controls the distribution of metals on smaller scales, which depends on the turbulent gas mixing and thus velocity dispersion. Thus, understanding global velocity dispersion structure could be key in studying the chemical evolution of galaxies and the distribution of metals and magnetic fields in the CGM.

3.5 Numerical aspects and nature of gas mixing

To understand the nature of mixing, it is essential to determine the numerical effects of the necessarily limited resolution in these simulations. The spatial resolution of the order of 1 kpc can limit the ability to capture the multi-phase nature of the CGM (Grønnow et al. 2018; Ji et al. 2019; Das & Gronke 2023), and thereby, small-scale physics (such as turbulence, magnetic fields, and fragmentation).
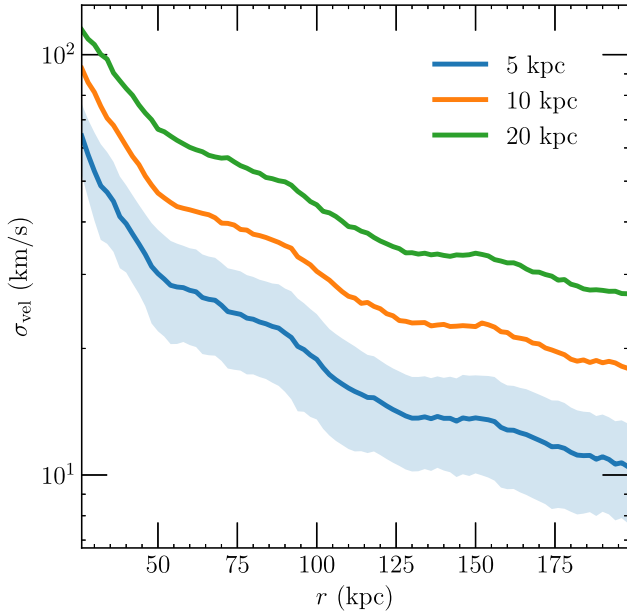
Figure 11. Velocity dispersion as a function of distance from the galactic centre (r). Three different characteristic length scales/diameters of the spherical regions (5, 10, 20 kpc) are used to calculate σ_{vel} by bootstrapping 100 samples of 100 data points at each r. The shaded blue region shows the scatter in σ_{vel} when evaluated on 5 kpc scales. σ_{vel} decreases radially and scales up with increasing characteristic lengths.

Therefore, we study the convergence behaviour of the gas mixing in our simulations.

To do this, we resimulate tracer dyes in the same halo with standard +2 kpcs spatial refinement and standard resolution (mass refinement only). The selection of dye locations follows the same methodology described in Section 2.2 to ensure choosing diverse environments for injecting the dye. The top panel of Fig. 12 shows $|\Delta_{\text{dye}}|$ against the average resolution of dyed cells after 200 Myr for all three simulations. The standard +1 kpc and standard +2 kpc runs have an almost fixed spatial resolution of 1 and 2 kpc, respectively, whereas the standard simulation has a range of cell sizes depending on their density.

A clear increase in $|\Delta_{\text{dye}}|$ is seen with worse resolutions in Fig. 12. The median of $|\Delta_{\text{dye}}|$ values for each resolution (shown in the bottom right of Fig. 12's top panel) also show this increasing trend. When going from 1 kpc resolution to 2 kpc, $|\Delta_{\text{dye}}|$ also increases twofold. This means that we are in a regime where the gas mixing is significantly affected by the numerical diffusion. That is why it is imperative to use the nearly fixed spatial resolution as we did here so that the dependence of gas mixing on physical properties is not due to spatial resolution variations that correlate with density in a mass refinement-only simulation. The standard resolution varies from $2 - 6$ kpc but $|\Delta_{\text{dye}}|$ shows a decreasing trend with lower spatial resolution (larger cell sizes). Because this simulation is refined on mass alone, the lower-resolution cells have lower densities. As we saw in Table 2, densities are correlated with σ_{vel}. Thus, lower resolution cells are on average located in regions with lower σ_{vel}, which leads to less mixing and balances the increase in numerical mixing.

The bottom panel of Fig. 12 shows the evolution of $|\Delta_{\text{dye}}|$ averaged over all dyes in each simulation over 200 Myr. To check the dependence of dye spread on the initial injection, we repeat our standard +1 kpc simulation but dye 8 neighbouring cells instead
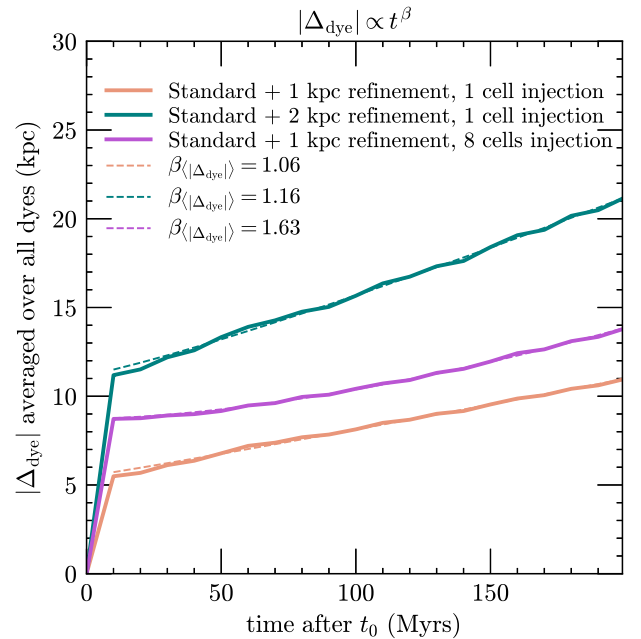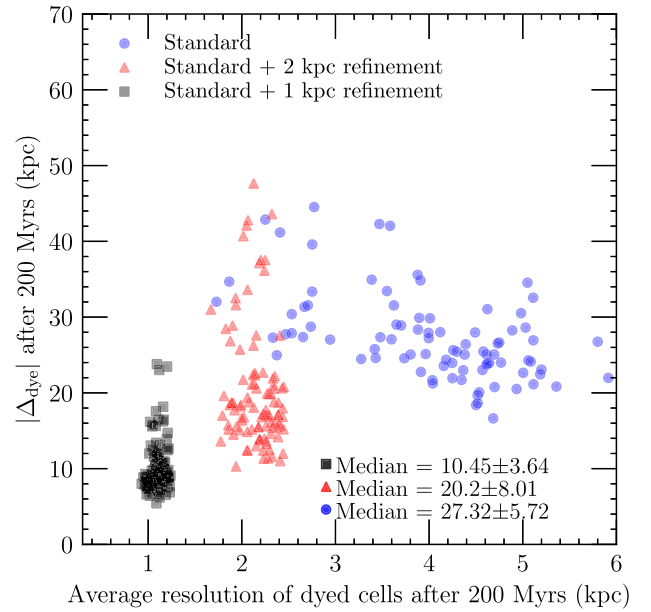
Figure 12. The top panel shows the magnitude of spread for all dyes 200 Myr after injection in different simulations as a function of the average resolution of dyed cells (dye mass fraction $> 10^{-7}$). Three different resolution simulations – standard (mass refinement), standard +2 kpc spatial refinement, and standard +1 kpc spatial refinement – are compared to study the effect of resolution on gas mixing. The legend in the bottom right corner shows each simulation's median of all $|\Delta_{\text{dye}}|$ values. An increasing trend in $|\Delta_{\text{dye}}|$ is seen with decreasing resolution. Note that throughout the paper, we have used Δ_{dye} from the standard +1 kpc run (black points). The Δ_{dye} for worse resolution cases is higher due to a higher velocity dispersion and larger impact of numerical mixing at those resolutions. The bottom panel shows the evolution of $|\Delta_{\text{dye}}|$ averaged over all dyes. The same 1 and 2 kpc simulation as in the top panel and an additional simulation with 1 kpc spatial refinement and a dye injection region of 8 neighbouring cells (as opposed to a single cell) are used to study the effects of both the size of the initial dye region and the resolution. A power law (mentioned in the title) is fitted to $|\Delta_{\text{dye}}|$ between $10 - 200$ Myr (to avoid the initial jump) by displacing $|\Delta_{\text{dye}}|$ such that it is zero at 10 Myr. The legend shows the exponent ($\beta_{\langle|\Delta_{\text{dye}}|\rangle}$) values for all three cases.

Table 4. This table shows the statistics of β for different simulations. (1 kpc, 1 cell), (2 kpc, 1 cell), and (1 kpc, 8 cells) refer to simulations with standard $+1$ kpc refinement with 1 cell injection, standard $+2$ kpc refinement with 1 cell injection, and standard $+1$ kpc refinement with 8 cells injection, respectively. $\beta_{\langle|\Delta_{\rm dye}|\rangle}$ is β calculated from the average dye spread, $\beta_{\rm Median}$ is median of β from all dye spreads, and $\beta_{\rm Mode}$ is the most probable β from all dye spreads assuming a bin size of 0.36 to create the PDF of β values.

Simulation	$\beta_{\langle|\Delta_{\rm dye}|\rangle}$	$\beta_{\rm Median}$	$\beta_{\rm Mode}$
(1 kpc, 1 cell)	1.06	0.94	0.76 ± 0.18
(2 kpc, 1 cell)	1.16	1.03	0.82 ± 0.18
(1 kpc, 8 cells)	1.63	1.42	1.16 ± 0.18

of a single cell as in our fiducial simulation, creating $(2\,{\rm kpc})^3$ clumps (similar to one cell at standard$+2$ kpc resolution) at ~ 1 kpc resolution. The jump in $|\Delta_{\rm dye}|$ seen in Fig. 12 at the first output time is due to the transfer of a significant amount of dye from the injection cells to adjacent cells, perhaps due to steep gradients in dye concentrations leading to higher numerical diffusion. Afterwards, the average $|\Delta_{\rm dye}|$, denoted as $\langle|\Delta_{\rm dye}|\rangle$, is proportional to $t^{\beta_{\langle|\Delta_{\rm dye}|\rangle}}$, where $\beta_{\langle|\Delta_{\rm dye}|\rangle} = 1.06, 1.16$, and 1.63 for one cell injection at 1 kpc, one cell injection at 2 kpc, and eight-cell injection at 1 kpc, respectively. We also look at the median and mode of β values for the individual 95 dyes in our sample. Mode is calculated as the most probable β from the PDF of β with a bin size of 0.36. All the values are summarized in Table 4.

For a normal diffusion (Brownian) process, $\beta = 0.5$. $\beta > 0.5$ suggests superdiffusion, and $\beta < 0.5$ suggests subdiffusion (Bouchaud & Georges 1990; Brandenburg, Käpylä & Mohammed 2004; Bakunin 2008). Our β values (Table 4) ranging from ~ 0.7 to 1.6 suggest that our simulations are strongly superdiffusive and in extreme cases hyperballistic ($\beta > 1.0$) over 200 Myr time-scales (Burnecki et al. 2015; Ilievski et al. 2021; Suzuki et al. 2022). Thus, the diffusion coefficient is not a constant quantity with time as it is in the case of normal diffusion. Such behaviour is expected from turbulent environments and large-scale coherent flow structures (Miesch, Brandenburg & Zweibel 2000), both present in the CGM. Additionally, the presence of numerical diffusion and limited dye statistics could also affect β. We find that some dyes have $\beta > 4$ (~ 4 per cent sample), leading to $\beta_{\langle|\Delta_{\rm dye}|\rangle} > \beta_{\rm Median} > \beta_{\rm Mode}$. This is caused by dyes with faster spread at later times due to a change in the environment (an increase in the velocity dispersion) rather than the nature of mixing. Thus, inferring the nature of mixing from the most probable or median β is more appropriate than using the average β skewed by some outliers. It should be noted that this diffusion behaviour could change when averaged over longer periods with more dyes. Thus, the superdiffusive behaviour of the dye might not apply to the general CGM.

Colbrook et al. (2017), for supersonic ISM turbulence, found a similar time-independent scale-dependent diffusivity $\kappa \approx 0.5 \mathcal{M}_{L_{\rm box}} (kL_{\rm box})^{-\alpha_c}$, where wavenumber $k = 2\pi/l$ describes variance on different scales, and $L_{\rm box}$ is the box scale at which the Mach number $\mathcal{M}$ is defined. We cannot reproduce the exact relations because of the lack of steady-state isotropic driven turbulence and 'Fourier diffusivity' analysis. We can still perform qualitative comparisons. In a 5 kpc box for our simulation, we find that

$$\langle {\rm DC} \rangle \propto \kappa \propto \Delta_{\rm dye}^2/t \propto \sigma_{\rm vel}^n. \qquad (16)$$

From Section 3.2, we know that $n \approx 1$; thus, $\kappa \propto \mathcal{M}$, same as Colbrook et al. (2017). And our time-dependent part $\Delta_{\rm dye}^2/t$ is potentially captured by their scale-dependent part $(kL_{\rm box})^{-\alpha_c}$ from

Fourier diffusivity analysis. Despite our inability to determine α_c as $\sigma_{\rm vel}$ and $\Delta_{\rm dye}$ are not independent, our results emphasize the need for a dynamic diffusivity model (scale- and/or time-dependent) even in the case of transonic CGM turbulence ($\mathcal{M}$ ranges from $\sim 0.2 - 1.2$ in our simulation).

Finally, for the numerical aspects of mixing, the standard $+2$ kpc run has the lowest resolution and the same amount of dye injection as the highest resolution 1 kpc run with eight cells injection. After the initial jump due to numerical reasons in Fig. 12 (bottom panel), both standard $+1$ kpc runs have the same rate of $\Delta_{\rm dye}$ increase, whereas the standard $+2$ kpc run shows an increase nearly double that. This again suggests that gas mixing at the resolution of our simulations is significantly affected by numerical diffusion. However, since we perform our study at a fixed spatial resolution, the dependence of gas mixing on the gas properties is likely not affected, even if the amount of mixing is. We explicitly tested the correlation results with standard $+2$ kpc resolution simulations and found qualitatively the same results.

3.6 Reynolds numbers for CGM turbulence

The numerical resolution of a simulation is critical for accurately capturing turbulence, which also affects gas mixing. To better understand the limitations of current simulations and their ability to capture turbulence, we calculate the physical and numerical Reynolds numbers (Re) at different distances from the centre (r) of the galaxy. The kinetic Reynolds number is defined as ${\rm Re} = \sigma_{\rm vel} l_{\rm D}/\nu$, where $\sigma_{\rm vel}$ is the velocity dispersion on a characteristic length-scale of $l_{\rm D} = 5$ kpc (see Figs 7 and 11), and ν is the kinematic viscosity (calculated from equation 3.16 in Brandenburg & Subramanian 2005, assuming fully collisional gas) with the following equation:

$$\nu = 1.3 \times 10^{23} \left(\frac{T}{10^6 \, {\rm K}} \right)^{5/2} \left(\frac{n_i}{{\rm cm}^{-3}} \right)^{-1} {\rm cm}^2 {\rm s}^{-1}. \qquad (17)$$

The volume-weighted average densities and temperatures in a 5 kpc box are used to calculate ν at a given r. Typical Re values for the inner ($50 < r/\,{\rm kpc} < 75$) and outer ($75 < r/\,{\rm kpc} < 200$) CGM are $\sim 10^3$ and 10^2, respectively (solid blue curve in Fig. 13), when we use the velocity dispersion at 5 kpc scales (see Fig. 11). For Kolmogorov turbulence, the effective numerical ${\rm Re} \approx N_{\rm grid}^{4/3}$ considering numerical viscosity (Schmidt 2015; Kriel et al. 2022; Shivakumar & Federrath 2025), where $N_{\rm grid}$ is the number of cells along one dimension in the turbulent region under consideration. We assume this because in subsonic turbulence, $\sigma_{\rm vel} \propto l^{1/3}$; thus, ${\rm Re} \propto l^{4/3}/\nu$. All the energy at grid scale is dissipated (${\rm Re} = 1$), which gives us $\nu \propto \Delta x^{4/3}$, where Δx is the grid resolution. The effective numerical ${\rm Re} \propto N_{\rm grid}^{4/3}$ follows from this, where the proportionality constant can be assumed to be ≈ 1 (Shivakumar & Federrath 2025). Thus, if a cell has a size of ~ 1 kpc, which is roughly the case here, we have only 5 cells in the region, and the numerical Re in that region is expected to be $\sim 5^{4/3} \sim 8$ (dashed blue curve in Fig. 13). The effective numerical Re quantifies the ability a simulation to resolve the physical Re. When the effective numerical Re of a simulation is equal to the physical Re, the numerical dissipation scale is the same as the viscous dissipation scale, and the turbulent cascade is modelled accurately.

Fig. 13 shows that physical Re is always greater than numerical Re, indicating that our simulations are numerically viscous. This leads to a loss of turbulent structures, as the dissipation occurs on larger scales than expected. The red curve shows the required resolution to match physical Re with the numerical Re. Resolution better than 1 kpc is needed to capture the full turbulent cascade in the simulations. While it may not be possible to capture the inner CGM
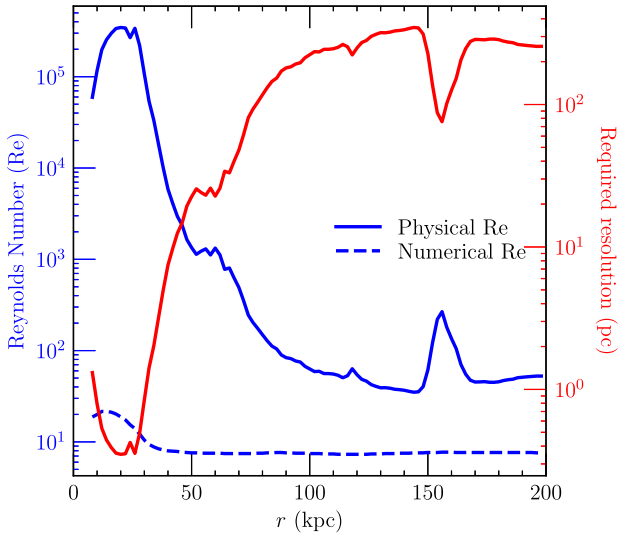
Figure 13. Left axis (blue) shows the physical Re (solid) and numerical Re (dashed), and the right axis (red) shows the resolution required for the physical Re to be equal to numerical Re (essentially, resolve turbulence) as a function of distance from the centre (r). The small peak/dip at ~ 150 kpc is due to the presence of a satellite galaxy. This graph suggests that we need a few hundred pc to resolve outer CGM turbulence beyond ~ 100 kpc (current resolution ~ 1 kpc).

turbulence in MW–mass galaxies (the resolution required is a few tens of pc or higher) in cosmological simulations, it is possible to capture turbulence in the outer CGM (≥ 75 kpc) with a resolution of a few hundred pc. This resolution may be where the convergence for gas mixing lies, because when we improve the resolution further, the effects of numerical viscosity would be less than the physical turbulent mixing. Understanding the limitations of current simulations and improving their accuracy in capturing turbulence could help to correctly interpret the gas properties, specifically the mixing and distribution of metals, which also affects gas cooling and gas accretion on to the central galaxy. Even though numerical diffusion is significant in our simulations, we have checked that our correlation results from Sections 3.1 and 3.3 remain valid at all resolutions.

4 CONCLUSIONS

In this study, we explore the mechanisms responsible for gas mixing in the CGM using cosmological, magnetohydrodynamical simulations conducted with the moving-mesh AREPO code. Most of our analysis is performed with simulations that have standard mass refinement plus a minimum spatial resolution of 1 kpc. We insert tracer dyes (passive scalars) in 95 locations representing diverse CGM environments – interacting inflow-outflow pairs, pure (coherent) inflows, pure (coherent) outflows, static gas, and outflows interacting with static flows. We track the evolution of the dye for 200 Myr to understand the nature of mixing. Our findings are summarized as follows:

(i) Interacting inflow–outflow pairs show a higher level of gas mixing with the surroundings than the pure coherent inflows and outflows. The static gas experiences similar levels of gas mixing to the pure coherent inflows and outflows.

(ii) To infer which gas property causes gas mixing, we perform the Spearman rank correlation test between the dye spread and

local gas properties such as temperature, metallicity, density, kinetic energy, magnetic field, velocity dispersion, symmetric shear tensor (or strain-rate tensor) magnitude, and antisymmetric shear tensor (or vorticity tensor) magnitude. We find that the velocity dispersion and traceless symmetric shear tensor (or pure shear deformation) magnitude (Smagorinsky 1963, see Section 3.1 for more details) correlate the best with dye spread. Thus, random and/or shearing motions likely cause gas mixing. Although not all SPH simulations include a subgrid model for metal diffusion, some SPH simulations estimate diffusivity using either velocity dispersion or symmetric shear tensors. Weaker, but still significant correlations are also found with other gas properties like density and kinetic energy, likely due to an underlying correlation with velocity dispersion.

(iii) When we correlate the dye spread after 200 Myr with local gas properties at different times in different-sized boxes around the dye location, we find that the correlation is maximal for velocity dispersion and symmetric shear tensor magnitudes measured in smaller regions (≤ 5 kpc) around dye injection locations ~ 70–120 Myr after dye injection. This implies that the impact of these velocity-derived quantities on gas mixing is largest after a ~ 100 Myr delay. We find that the diffusion coefficient calculated from dye spread has a nearly linear dependence on the velocity dispersion with a power-law exponent of 1.1 ± 0.09 (robust to changes in resolution). Scaling constants range from 0.1 to 0.6 when estimating diffusion using velocity dispersion, and the Smagorinsky constants vary from 0.2 to 0.4 when estimating diffusion from shear tensors. These numerical simulation results from implicit modelling of gas mixing can be useful to estimate diffusion in explicit subgrid models employed by some SPH simulations (Klessen & Lin 2003; Greif et al. 2009; Williamson et al. 2016).

(iv) Our alignment analysis reveals that velocity and magnetic field dispersion both correlate with the dyed cloud's shape. However, vectors calculated from the traceless symmetric shear tensor and antisymmetric shear tensor exhibit a stronger alignment. Specifically, the dispersion of stretching (deformation) eigenvectors of the symmetric shear tensors and plane-of-rotation eigenvectors of the antisymmetric shear tensors shows the maximum alignment with the dye shape. Nearly, 70 per cent of our dye sample has stretching eigenvectors' dispersion and dye spread direction aligned to within 9.6 deg. The shape of the dye spread correlates best with gas properties measured in larger boxes (≥ 10 kpc) contrary to the correlation of the extent of mixed dye, which is larger in smaller boxes (0–5 kpc). Overall, we find that traceless symmetric shear tensors best predict the extent and shape of gas mixing in our simulations, slightly better than velocity dispersion.

(v) We find that numerical mixing plays an important role in our simulations. When we change the refinement criterion of fixed spatial resolution from 1 to 2 kpc, the dye spreads twice as quickly. However, despite the amount of gas mixing changing, the strong qualitative correlation with velocity dispersion remains.

(vi) The velocity dispersion decreases with increasing galactocentric radius. This implies a reduction in gas mixing further out in the CGM, useful for understanding metal diffusion (Nugent et al. 2025). Velocity dispersion can be used to compute Reynolds numbers in the CGM. The inner ($50 < r/\mathrm{kpc} < 75$) and outer ($75 < r/\mathrm{kpc} < 200$) CGM have typical values of $\sim 10^3$ and 10^2, respectively. We find that the numerical resolution is not enough to resolve the physical Reynolds numbers. In order to resolve turbulence in the outer CGM, the required resolution would be a few hundred pc for the outer CGM ($r > 75$ kpc) and a few tens of pc or smaller for the inner CGM.

(vii) The dye spread exhibits a power-law dependence with time, having most exponents ranging from ~ 0.7 to 1.1. In normal (Brow-

nian) diffusion, a square root time dependence (exponent ~ 0.5) is expected. Thus, we have a case of superdiffusion or hyperballistic diffusion over 200 Myr time-scales, which could be caused by turbulence, large-scale coherent flows, and numerical diffusion in the CGM. Thus, the diffusion coefficient is a time-varying quantity in our simulations.

Despite the inability of our cosmological simulations to capture the full cascade of turbulence in the CGM, a fixed spatial resolution in the CGM aids us in filtering out the numerical effects on gas mixing. Although the amount of gas mixing is not converged with resolution, the differences we found in gas mixing in different physical environments were found to be robust. Thus, our findings that the amount and the direction of gas mixing correlate the best with velocity dispersion and symmetric shear tensors hold, irrespective of the resolution. These results help us understand the fundamental nature of gas and metal diffusion in the CGM, which is crucial to understanding the gas flows into and out of galaxies and the distribution of metals in the CGM. The topic of multiphase turbulent mixing is complex and many unanswered questions remain, such as the impact of magnetic fields, and whether we can fully resolve CGM turbulence and obtain converged results. We plan to tackle these questions in the future.

ACKNOWLEDGEMENTS

DATA AVAILABILITY

Data related to this work will be shared on reasonable request to the corresponding author.

REFERENCES

Amaral A. D., Vernstrom T., Gaensler B. M., 2021, MNRAS, 503, 2, 2913–2926

Arámburo-García A., Bondarenko K., Boyarsky A., Neronov A., Scaife A., Sokolenko A., 2023, MNRAS, 519, 4030

Armillotta L., Fraternali F., Werk J. K., Prochaska J. X., Marinacci F., 2017, MNRAS, 470, 114

Bakunin O. G., 2008, Turbulence and Diffusion. Springer, Berlin, Heidelberg, p. XVI

Banda-Barragán W. E., Federrath C., Crocker R. M., Bicknell G. V., 2018, MNRAS, 473, 3454

Bauer A., Springel V., 2012, MNRAS, 423, 2558

Beattie J. R., Federrath C., Kriel N., Hew J. K. J., Bhattacharjee A., 2025, Taking Control of Compressible Modes: Bulk Viscosity and the Turbulent Dynamo. preprint (arXiv:2312.03984).

Beck A. M., Lesch H., Dolag K., Kotarba H., Geng A., Stasyszyn F. A., 2012, MNRAS, 422, 2152

Begelman M. C., Fabian A. C., 1990, MNRAS, 244, 26P

Behroozi P. S., Conroy C., Wechsler R. H., 2010, ApJ, 717, 379

Bernet M. L., Miniati F., Lilly S. J., 2013, ApJ, 772, L28

Bigiel F. et al., 2011, ApJ, 730, L13

Böckmann K. et al., 2023, A&A, 678, A56

Bouchaud J.-P., Georges A., 1990, Phys. Rep., 195, 127

Brandenburg A., Subramanian K., 2005, Phys. Rep., 417, 1

Brandenburg A., Käpylä P. J., Mohammed A., 2004, Phys. Fluids, 16, 1020

Brook C. B., Stinson G., Gibson B. K., Shen S., Macciò A. V., Obreja A., Wadsley J., Quinn T., 2014, MNRAS, 443, 3809

Burnecki K., Kepten E., Garini Y., Sikora G., Weron A., 2015, Sci. Rep., 5, 11306

Chandrasekhar S., 1968, Hydrodynamic and Hydromagnetic Stability. Clarendon Press, United States

Christensen C. R., Davé R., Brooks A., Quinn T., Shen S., 2018, ApJ, 867, 142

Clark R. A., Ferziger J. H., Reynolds W. C., 1979, J. Fluid Mech., 91, 1

Colbrook M. J., Ma X., Hopkins P. F., Squire J., 2017, MNRAS, 467, 2421

Crain R. A., van de Voort F., 2023, ARA&A, 61, 473

Dale J. E., 2015, New A Rev., 68, 1

Das H. K., Gronke M., 2023, MNRAS, 527, 991

Das S., Mathur S., Gupta A., Krongold Y., 2021, ApJ, 918, 83

Duffell P. C., MacFadyen A. I., 2011, ApJS, 197, 15

Escala I. et al., 2018, MNRAS, 474, 2194

Faucher-Giguere C.-A., P. Oh S., 2023a, Annual Review of Astronomy and Astrophysics. Key Physical Processes in the Circumgalactic Medium. Annual Reviews, 131–195, https://www.annualreviews.org/content/journals/10.1146/annurev-astro-052920-125203

Faucher-Giguère C.-A., Oh S. P., 2023b, ARA&A, 61, 131

Federrath C., Klessen R. S., 2012, ApJ, 761, 156

Federrath C., Roman-Duval J., Klessen R. S., Schmidt W., Mac Low M., 2010, A&A, 512, A81

Federrath C., Klessen R. S., Iapichino L., Beattie J. R., 2021, Nat. Astron., 5, 365

Fielding D., Quataert E., McCourt M., Thompson T. A., 2017, MNRAS, 466, 3810

Fox A. J., Wakker B. P., Smoker J. V., Richter P., Savage B. D., Sembach K. R., 2010, ApJ, 718, 1046

Fukugita M., Peebles P. J. E., 2006, ApJ, 639, 590

Fukugita M., Hogan C. J., Peebles P. J. E., 1998, ApJ, 503, 518

Gaensler B. M., Madsen G. J., Chatterjee S., Mao S. A., 2008, PASA, 25, 184

Garnier E., Adams N., Sagaut P., 2009, Large Eddy Simulation for Compressible Flows. Springer, the Netherlands, http://dx.doi.org/10.1007/978-90-481-2819-8

Germano M., Piomelli U., Moin P., Cabot W. H., 1991, Phys. Fluids A: Fluid Dyn., 3, 1760

Grand R. J. J. et al., 2017, MNRAS, 467, 179

Grand R. J. J. et al., 2019, MNRAS, 490, 4786

Grand R. J. J. et al., 2021, MNRAS, 507, 4953

Greif T. H., Glover S. C. O., Bromm V., Klessen R. S., 2009, MNRAS, 392, 1381

Grønnow A., Tepper-García T., Bland-Hawthorn J., 2018, ApJ, 865, 64

Grudić M. Y., 2022, meshoid: A Meshless Finite-volume Code for Hydrodynamics, https://github.com/mikegrudic/meshoid

Hafen Z. et al., 2020, MNRAS, 494, 3581

Harris C. R. et al., 2020, Nature, 585, 357

Heavens A., Panter B., Jimenez R., Dunlop J., 2004, Nature, 428, 625

Heesen V. et al., 2023, A&A, 670, L23

Heyer M. H., Brunt C. M., 2004, ApJ, 615, L45

Hopkins P. F. et al., 2018, MNRAS, 480, 800

Huang S., Katz N., Cottle J., Scannapieco E., Davé R., Weinberg D. H., 2022, MNRAS, 509, 6091

Hummels C. B. et al., 2019, ApJ, 882, 156

Hunter J. D., 2007, Comput. Sci. Eng., 9, 90

Ilievski E., De Nardis J., Gopalakrishnan S., Vasseur R., Ware B., 2021, Phys. Rev. X, 11, 031023

Jennings F., Beckmann R. S., Sijacki D., Dubois Y., 2023, MNRAS, 518, 5215

Ji S., Oh S. P., Masterson P., 2019, MNRAS, 487, 737

Kacprzak G. G., Churchill C. W., 2011, ApJ, 743, L34

Kemenov K. A., Wang H., Pope S. B., 2011, Flow, Turbulence and Combustion, 88, 529

Kennicutt R. C., Evans N. J., 2012, ARA&A, 50, 531

Klessen R. S., Lin D. N. C., 2003, Phys. Rev. E, 67, 046311

Kriel N., Beattie J. R., Seta A., Federrath C., 2022, MNRAS, 513, 2457

Kritsuk A. G., Norman M. L., Padoan P., Wagner R., 2007, ApJ, 665, 416

Kwak K., Henley D. B., Shelton R. L., 2011, ApJ, 739, 30

Lan T.-W., Prochaska J. X., 2020, MNRAS, 496, 3142

Landau L., Lifshitz E., 2013, Fluid Mechanics: Volume 6. Pergamon, https://books.google.com.au/books?id=CeBbAwAAQBAJ

Larson R. B., 1981, MNRAS, 194, 809

Leonard A., 1975, in Frenkiel F., Munn R., eds, Advances in Geophysics, Vol. 18, Turbulent Diffusion in Environmental Pollution. Elsevier, p. 237, https://doi.org/10.1016/S0065-2687(08)60464-1

Lesieur M., Metais O., 1996, Ann. Rev. Fluid Mech., 28, 45, https://doi.org/10.1146/annurev.fl.28.010196.000401

Locatelli N. et al., 2024, A&A, 681, A78

Marinacci F., Vogelsberger M., Mocz P., Pakmor R., 2015, MNRAS, 453, 4000

Mastropietro C., Moore B., Mayer L., Wadsley J., Stadel J., 2005, MNRAS, 363, 509

McCourt M., Sharma P., Quataert E., Parrish I. J., 2012, MNRAS, 419, 3319

McGaugh S. S., Schombert J. M., de Blok W. J. G., Zagursky M. J., 2009, ApJ, 708, L14

Meneveau C., Katz J., 2000, Ann. Rev. Fluid Mech., 32, 1, https://doi.org/10.1146/annurev.fluid.32.1.1

Miesch M. S., Brandenburg A., Zweibel E. G., 2000, Phys. Rev. E, 61, 457

Miller M. J., Bregman J. N., 2015, ApJ, 800, 14

Mitchell P. D., Schaye J., Bower R. G., Crain R. A., 2020, MNRAS, 494, 3971

Mohapatra R., Jetti M., Sharma P., Federrath C., 2021a, MNRAS, 510, 2327

Mohapatra R., Jetti M., Sharma P., Federrath C., 2021b, MNRAS, 510, 3778

Murante G., Monaco P., Borgani S., Tornatore L., Dolag K., Goz D., 2014, MNRAS, 447, 178

Muratov A. L. et al., 2017, MNRAS, 468, 4170

Nugent A. E., Ji A. P., Fong W.-f., Shah H., van de Voort F., 2025, The Astrophysical Journal, 982, 144

Oppenheimer B. D., Davé R., Kereš D., Fardal M., Katz N., Kollmeier J. A., Weinberg D. H., 2010, MNRAS, 406, 2325

Pakmor R., Springel V., Bauer A., Mocz P., Munoz D. J., Ohlmann S. T., Schaal K., Zhu C., 2015, MNRAS, 455, 1134

Pakmor R. et al., 2017, MNRAS, 469, 3185

Pakmor R. et al., 2020, MNRAS, 498, 3125

Pan L., Scannapieco E., Scalo J., 2012, Journal of Fluid Mechanics, 700, 459

Peeples M. S., Werk J. K., Tumlinson J., Oppenheimer B. D., Prochaska J. X., Katz N., Weinberg D. H., 2014, The Astrophysical Journal, 786, 54

Peeples M. S. et al., 2019, ApJ, 873, 129

Piomelli U., Liu J., 1995, Physics of Fluids, 7, 839

Planck Collaboration et al., 2014, A&A, 571, A16

Prandtl L., 1925, ZAMM—Journal of Applied Mathematics and Mechanics/Zeitschrift für Angewandte Mathematik und Mechanik, 5, 136, https://doi.org/10.1002/zamm.19250050212

Putman M. E., 2017, Gas Accretion onto Galaxies. Springer International Publishing, p. 1, https://doi.org/10.1007/978-3-319-52512-9_1

Ramesh R., Nelson D., Heesen V., Brüggen M., 2023, MNRAS, 526, 5483

Rennehan D., 2021, MNRAS, 506, 2836

Rennehan D., Babul A., Hopkins P. F., Davé R., Moa B., 2019, MNRAS, 483, 3810

Reynolds O., 1895, Phil. Trans. R. Soc. London, 186, 123

Rogallo R. S., Moin P., 1984, Ann. Rev. Fluid Mech., 16, 99

Roy M., Su K.-Y., Tonnesen S., Fielding D. B., Faucher-Giguère C.-A., 2024, MNRAS, 527, 265

Saeedzadeh V. et al., 2023, MNRAS, 525, 5677

Sagaut P., 2006, Large Eddy Simulation for Incompressible Flows. Springer, Berlin, Heidelberg, http://dx.doi.org/10.1007/b137536

Scannapieco E., Brüggen M., 2015, ApJ, 805, 158

Schmidt W., 2015, Living Rev. Comput. Astrophys., 1

Schmitt F. G., 2007, Comptes Rendus. Mécanique, 335, 617

Schneider E. E., Robertson B. E., 2017, ApJ, 834, 144

Schneider E. E., Ostriker E. C., Robertson B. E., Thompson T. A., 2020, ApJ, 895, 43

Seta A., Federrath C., 2021, Phys. Rev. Fluids, 6, 103701

Seta A., Federrath C., 2022, MNRAS, 514, 957

Seta A., Bushby P. J., Shukurov A., Wood T. S., 2020, Phys. Rev. Fluids, 5, 043702

Shah H., Seta A., 2021, MNRAS, 508, 1371

Shen S., Wadsley J., Stinson G., 2010, MNRAS, 407, 1581

Shen S., Madau P., Aguirre A., Guedes J., Mayer L., Wadsley J., 2012, ApJ, 760, 50

Shen S., Madau P., Guedes J., Mayer L., Prochaska J. X., Wadsley J., 2013, ApJ, 765, 89

Shivakumar L. M., Federrath C., 2025, MNRAS, 537, 2961

Shull J. M., Jones J. R., Danforth C. W., Collins J. A., 2009, ApJ, 699, 754

Sijacki D., Vogelsberger M., Kereš D., Springel V., Hernquist L., 2012, MNRAS, 424, 2999

Smagorinsky J., 1963, Monthly Weather Rev., 91, 99

Sokołowska A., Babul A., Mayer L., Shen S., Madau P., 2018, ApJ, 867, 73

Sparre M., Pfrommer C., Vogelsberger M., 2018, MNRAS, 482, 5401

Spitzer Lyman J., 1956, ApJ, 124, 20

Springel V., 2010, MNRAS, 401, 791

Steidel C. C., Erb D. K., Shapley A. E., Pettini M., Reddy N., Bogosavljević M., Rudie G. C., Rakic O., 2010, ApJ, 717, 289

Stern J., Fielding D., Faucher-Giguère C.-A., Quataert E., 2019, MNRAS, 488, 2549

Stinson G. S. et al., 2012, MNRAS, 425, 1270

Suzuki J. L., Gulian M., Zayernouri M., D'Elia M., 2022, J. Peridynamics Nonlocal Modeling, 5, 392

Thompson T. A., Quataert E., Zhang D., Weinberg D. H., 2015, MNRAS, 455, 1830

Tremmel M., Karcher M., Governato F., Volonteri M., Quinn T. R., Pontzen A., Anderson L., Bellovary J., 2017, MNRAS, 470, 1121

Tremonti C. A. et al., 2004, ApJ, 613, 898

Tumlinson J. et al., 2011, ApJ, 733, 111

Tumlinson J., Peeples M. S., Werk J. K., 2017, ARA&A, 55, 389

Valdarnini R., 2011, A&A, 526, A158

van de Voort F., Bieri R., Pakmor R., Gómez F. A., Grand R. J. J., Marinacci F., 2021, MNRAS, 501, 4888

van de Voort F., Pakmor R., Grand R. J. J., Springel V., Gómez F. A., Marinacci F., 2020, MNRAS, 494, 4867

van de Voort F., Springel V., Mandelker N., van den Bosch F. C., Pakmor R., 2019, MNRAS, 482, L85
Virtanen P. et al., 2020, Nature Methods, 17, 261
Wadsley J. W., Veeravalli G., Couchman H. M. P., 2008, MNRAS, 387, 427
Wadsley J. W., Keller B. W., Quinn T. R., 2017, MNRAS, 471, 2357
Wakker B. P., van Woerden H., 1997, ARA&A, 35, 217
Wakker B. P. et al., 2007, ApJ, 670, L113
Weinberger R., Springel V., Pakmor R., 2020, ApJS, 248, 32
Werk J. K. et al., 2014, ApJ, 792, 8
Williamson D., Martel H., Kawata D., 2016, ApJ, 822, 91

APPENDIX A: INTERACTING INFLOW–OUTFLOW SELECTION METHODOLOGY

To find interacting inflows–outflows (*io*), first, we look for all inflow and outflow voxels (see Fig. 1) whose centres are within $20\sqrt{3}$ kpc ($2\times$ voxel diagonal) of one another, where voxels represent $10 \times 10 \times 10$ kpc gas regions. This is done to narrow down the adjacent (potentially interacting) voxels, as we aim to find two regions of gas that are likely to interact in the near future. We then locate the points on both voxel centre trajectories where the closest approach occurs. As the shortest distance is perpendicular to both trajectories, it can be found using

$$\vec{r}_1^v + t_1 \vec{V}_1^v + t_3(\vec{V}_1^v \times \vec{V}_2^v) = \vec{r}_2^v + t_2 \vec{V}_2^v, \tag{A1}$$

where 1 and 2 denote an inflow and outflow voxel, respectively, $\vec{r}_{1/2}^p$ are their position vectors, and $\vec{V}_{1/2}^p$ are their velocity vectors. The equation can be solved for t_1, t_2, and t_3. As the interaction will happen in the direction of the respective velocity vectors, only positive values of t_1 and t_2 are considered valid. The points of the closest approach also have to be near the initial voxel positions on the simulation time-scale of 200 Myr. Thus, we make sure that the distance between the initial voxel positions and the respective points of closest approach is smaller than the distance a voxel would travel in 150 Myr at the current speed. Furthermore, the distance between the points of closest approach has to be smaller than 10 kpc, i.e. the voxel size.

Lastly, to ensure interaction, both voxels must reach their respective points of closest approach nearly simultaneously. Fig. A1 shows one extreme case where an interaction between the voxels is considered to be just possible (bottom edges of the faster blue voxel and slower black voxel just touch). In this extreme case, the time taken from the initial to interaction state (traced out from trajectories of voxels assuming constant velocities) would be the same for both voxels, which can be expressed as

$$\frac{d_1 + (L/2)\tan(\alpha/2)}{V_1^v} = \frac{d_2 - (L/2)\tan(\alpha/2)}{V_2^v}, \tag{A2}$$

where d_1 and d_2 are distances from initial voxel positions to voxel positions at the point of closest approach, $L = 10$ kpc is the width of a voxel, and α is the angle between the voxel trajectories. equation A2 can be expressed as

$$\left| \frac{d_1}{V_1^v} - \frac{d_2}{V_2^v} \right| = \frac{L}{2}\tan(\alpha/2)\left(\frac{1}{V_1^v} + \frac{1}{V_2^v} \right) \tag{A3}$$

The left-hand side (LHS) of this equation represents the absolute difference in time taken by the voxels to reach their respective points of closest approach. Thus, the two voxels could interact if the LHS is smaller than the right-hand side.
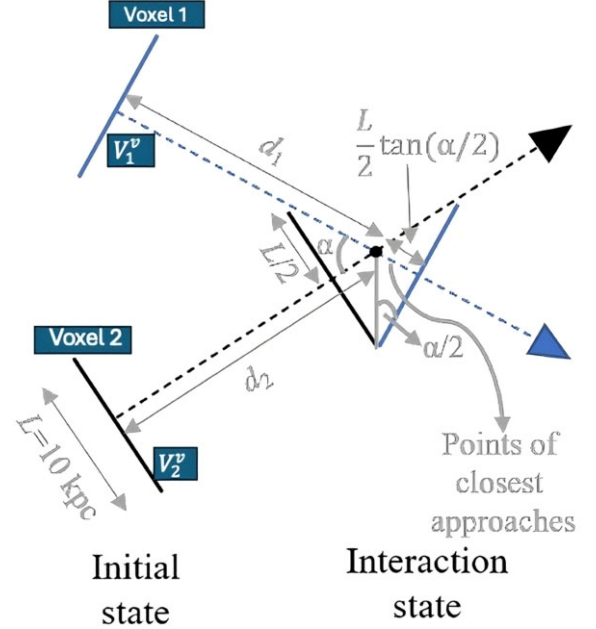

Figure A1. Top-view (along $V_1^v \times V_2^v$) schematic of two voxels (shown as 1D voxel cross-sections) represented by a blue and a black line ($10 \times 10 \times 10$ kpc) in the CGM headed towards each other. The interaction state shown here is an extreme case of voxel interaction (where voxels barely overlap) after assuming their velocities to remain constant. Blue and black colours are used with voxels 1 and 2, respectively. Points of the closest approach, overlapping from the top view, represent the shortest distance between the trajectories of both voxels.

APPENDIX B: GAS PROPERTY AND RESOLUTION TEST PLOTS

Fig. B1 shows the mean (solid curves) and standard deviation (shaded regions) of the velocity dispersion, kinetic energy density, and overdensity around all the dyes in regions of different sizes at different times. Velocity dispersion scales with box size to the power 0.5, while kinetic energy density and overdensity remain constant. The mean remains constant with time, while the scatter increases for kinetic energy density and overdensity. This shows that some dyes undergo major changes with time, but the general environmental character remains constant when averaging over all cases.

Fig. B2 shows the Spearman rank (r_s) correlation coefficient between dye spread and velocity dispersion, kinetic energy density, and overdensity averaged over different box sizes around the dyes at different times. The dye is initially injected in clumps of eight cells for Fig. B2, while it was injected in single cells for Fig. 7. The velocity dispersion still correlates best with the spread of the dye (maximum $r_s \sim 0.86$) and the results remain very similar to one-cell injection. The peak in r_s is attained slightly earlier, however, possibly due to dye spreading out to optimal configuration for transfer of velocity dispersion to spread faster.
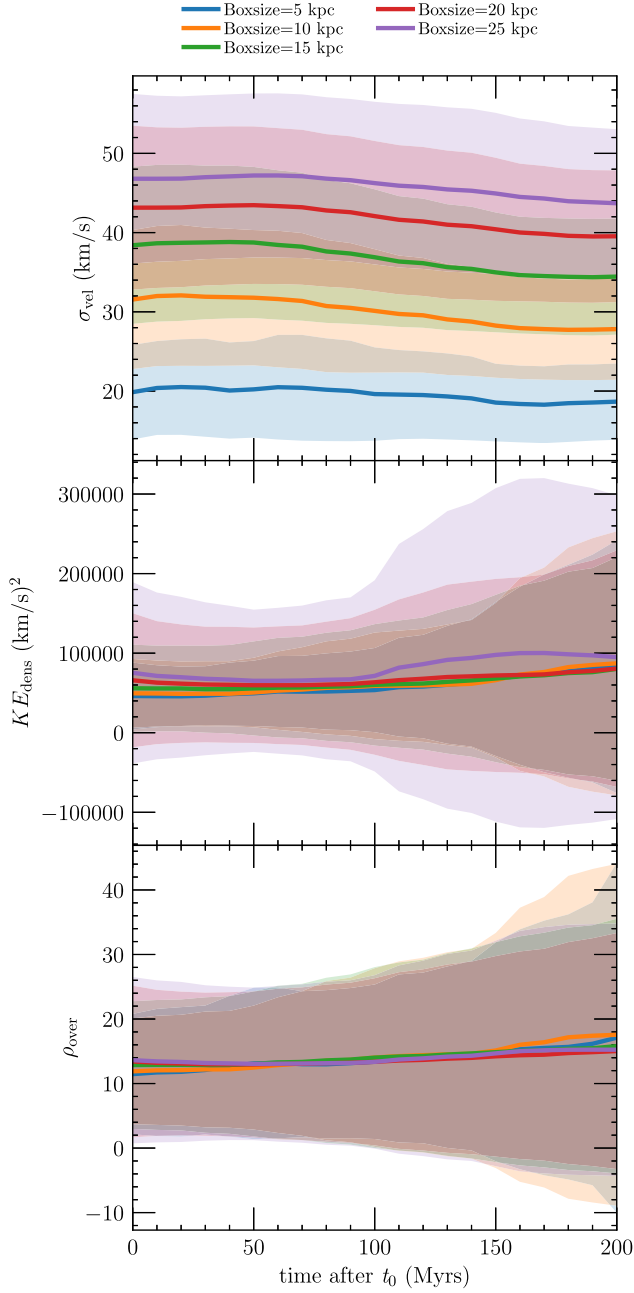
Figure B1. Gas properties averaged over different boxes (with varying sizes) around the dye injection locations as a function of time after injection. The solid lines and the shaded regions around them show the mean and the standard deviation of the data set, respectively. The velocity dispersion remains constant with time, but scales to the power of ~ 0.5 with box size. Mean kinetic energy density and overdensity remain roughly constant with time and box size. Despite all gas properties varying minimally with time, the gas property exhibiting direct correlation with dye spread might still have varying correlation strengths temporally.
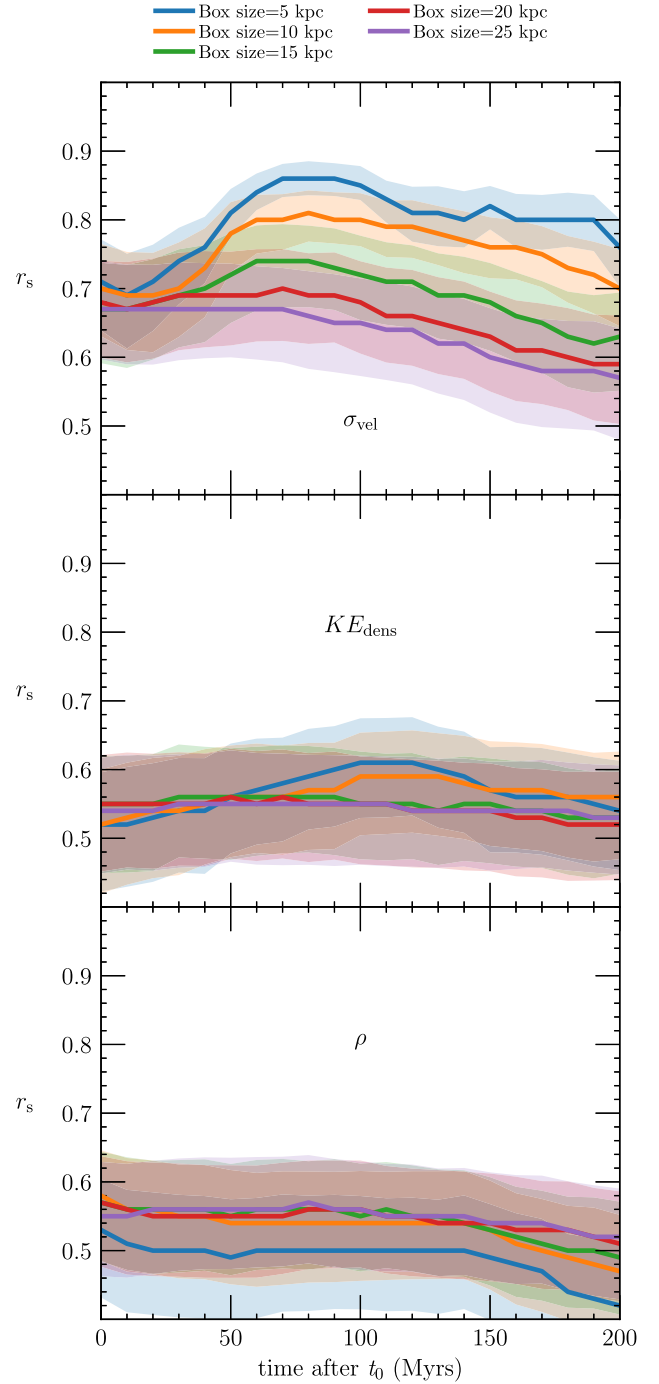
Figure B2. Spearman rank coefficient (r_s) of the correlation between the magnitude of dye spread after 200 Myr and averaged gas properties in boxes around the dye injection locations with different sizes at different times. The errorbars represent 1σ confidence intervals from bootstrapping the sample 10 000 times. This is the same graph as Fig. 7 but with an eight-cell dye injection at each location instead of one.

This paper has been typeset from a TeX/LaTeX file prepared by the author.